Geophysical Journal International

Geophys. J. Int. (2014) **196,** 1330–1350
Advance Access publication 2013 December 20

doi: 10.1093/gji/ggt455

Three-dimensional electrical conductivity structure beneath Australia from inversion of geomagnetic observatory data: evidence for lateral variations in transition-zone temperature, water content and melt

Takao Koyama,[1,*] Amir Khan[1,2] and Alexey Kuvshinov[1]

[1]*Institute of Geophysics, Swiss Federal Institute of Technology, Zürich, Switzerland. E-mail: tkoyama@eri.u-tokyo.ac.jp*
[2]*Institute of Geochemistry and Petrology, Swiss Federal Institute of Technology, Zürich, Switzerland*

Accepted 2013 November 6. Received 2013 September 13; in original form 2013 May 24

SUMMARY

In this paper, we report the 3-D electrical conductivity distribution beneath the Australian continent in the depth range 410–1600 km, which we have imaged by inverting *C*-response estimates from a regional network of geomagnetic observatories. The inversion scheme is based on a quasi-Newton optimization method while the forward algorithm relies on an integral-equation approach. To properly account for the ocean effect in responses at coastal observatories we included a high-resolution ($1^\circ \times 1^\circ$) fixed thin laterally varying surface conductance layer. As starting model in the inversion we considered a laboratory-based 3-D conductivity model of the region obtained from seismic surface wave data and thermodynamic modelling. This model provides a good fit to observed *C*-response estimates supporting its choice as initial model. The most striking feature of the obtained 3-D model is a high-conductivity anomaly in the lower part of the mantle transition zone (MTZ; 520–660 km depth) beneath southeastern Australia implying considerable lateral as radial heterogeneity in the conductivity structure. The high-conductivity region appears to be 0.5–1 log units more conductive than previous global and other regionalized 1-D models. Further analysis using laboratory-based conductivity models combined with thermochemical phase equilibrium computations shows that the strong conductivity anomaly implies water contents of around 0.1 wt per cent in the upper part and >0.4 wt per cent in the lower part of the MTZ. This implies a large MTZ water reservoir that likely totals one to three times that which currently resides in the oceans. The amount of water in the lower MTZ appears to exceed the experimentally determined water storage capacity of the main lower MTZ mineral ringwoodite, which, as a result, undergoes dehydration-induced partial melting. Including contributions to conductivity from a thin melt layer (20 km thick) located in the mid-MTZ increases conductivity locally in the melt layer to ~ 1 S m^{-1}, that is, about 0.5 log units more conductive than the average surrounding mantle. This provides an adequate explanation for the strong conductivity anomalies observed beneath part of the continent and points to lateral variations in melt in the MTZ.

Key words: Numerical solutions; Inverse theory; Electrical properties; Geomagnetic induction; Composition of the mantle; Phase transitions.

1 INTRODUCTION

Geophysical studies, particularly those centred on seismology and seismic tomography, have revealed a variety of heterogeneous mantle structures comprising length scales from small range (km sized) to continental scale (e.g. Helffrich & Wood 2001; Kustowski *et al.* 2008) that bear evidence of the complex dynamics that have shaped mantle structure. In spite of many advances (Rawlinson *et al.* 2010) and a consensus that the underlying processes responsible for the observed velocity variations are related to thermochemical variations, seismology has yet to provide a clear picture of the origin of these heterogeneities (e.g. Trampert & Van der Hilst 2005; Khan *et al.* 2009).

In an attempt to overcome this we seek to investigate properties that, in principle, are more sensitive to the main parameters of interest, that is, composition and temperature, than is elasticity. Electrical conductivity is one of the characteristic physical parameters of materials composing the Earth's interior and depends strongly on the number of free charge carriers and their mobility (e.g. Poirier 2000;

*On leave from: Earthquake Research Institute, University of Tokyo, Japan.

Karato & Wang 2012) and is therefore sensitive to variations of state variables such as temperature, chemical composition, oxygen fugacity, water content and melt (e.g. Shankland *et al.* 1981; Roberts & Tyburczy 1999; Park & Ducea 2003; Frost & McCammon 2008; Yoshino 2010; Karato 2011; Khan & Shankland 2012, among others). As a result, estimating mantle electrical conductivity structure is a potentially strong tool for mapping mantle chemistry, mineralogy and physical structure and presents a complementary method to seismic studies that seek to elucidate the elastic properties of the mantle.

On a global scale 3-D electromagnetic (EM) induction studies of long-period geomagnetic data (Kelbert *et al.* 2009; Tarits & Mandea 2010; Semenov & Kuvshinov 2012), like their seismic counterparts, reveal a substantial level of lateral heterogeneity in the mantle (depth range 410–1600 km). Particularly, underneath Australia, regions of enhanced conductivity (0.5–1 S m^{-1}) are discernable in the mantle transition zone (MTZ). If real, these anomalous conductivity regions (compared with 'normal' MTZ conductivities that lie in the range 0.01–0.3 S m^{-1}) imply substantial differences in mantle thermochemistry (e.g. Verhoeven *et al.* 2009; Khan *et al.* 2011a) volatile content such as water (e.g. Yoshino 2010; Karato 2011), differing redox conditions (e.g. Dai *et al.* 2012) and/or presence of melt (e.g. Toffelmier & Tyburczy 2007; Mookherjee *et al.* 2008; Khan & Shankland 2012).

Given the relevance of these parameters in constraining such critical processes as chemical differentiation and geodynamical evolution, assessment of any such conductivity anomalies is highly important. However, the limited resolution of current global 3-D conductivity models precludes verification of structures on regional or subregional scales. In this paper, we report the results of a regional-scale 3-D EM inversion of geomagnetic data from Australian observatories applying the method of Koyama *et al.* (2006) in order to delineate more precisely the MTZ conductivity structure beneath the Australian continent. Previous Australian deep EM studies were only aimed at sounding the upper mantle (e.g. Campbell *et al.* 1998; Wang & Lilley 1999; Simpson 2001; Heinson & White 2005; Ichiki *et al.* 2012, among others).

As with any non-linear inverse problem the choice of starting model is very important. Here we take a novel approach by employing a 3-D conductivity model, which has been obtained from a combination of a regional seismic tomography study of the Australian continent (Khan *et al.* 2013) with thermodynamic computations of mantle minerals, and laboratory-based conductivity measurements. This initial conductivity model thus has the advantage of being closely linked to seismic tomography, while at the same time being grounded in experimental measurements, and, as will be shown in the following, provides a good fit to observations.

Based on this smooth initial conductivity model we performed a 3-D EM inversion using the data from eight geomagnetic stations distributed across the Australian continent. The inverted model reveals a relatively strong conductivity anomaly in the MTZ beneath southeastern Australia that is 0.5–1 log unit more conductive than the surrounding mantle. The observed conductivity variations indicate considerable lateral and radial heterogeneity in mantle structure. To further ascertain the robustness of the obtained 3-D conductivity model, extensive model studies are conducted and discussed. A final section provides detailed interpretation of the recovered subcontinental Australian conductivity structure in the light of recent experimental conductivity measurements and laboratory-based conductivity profiles. The analysis performed in this section strongly suggests that the MTZ conductivity anomaly beneath Australia reflects lateral variations in temperature, water content and melt. Details of forward and inverse methodologies are supplied in the Appendices.

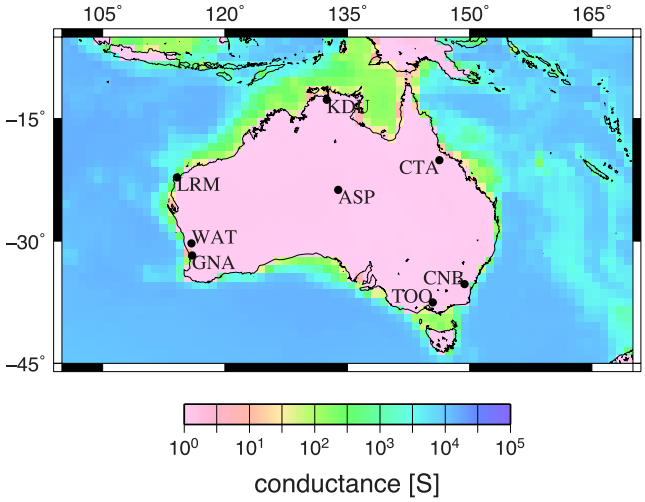

Figure 1. Conductance map showing non-uniform thin surface layer employed in this study. Station names and locations are also indicated (for details see Table 1).

2 DATA

The data with which we work are local C-responses, which are determined from (e.g. Banks 1969)

$$C(\mathbf{r}_a, \omega) = -\frac{a \tan \vartheta}{2} \frac{Z(\mathbf{r}_a, \omega)}{H(\mathbf{r}_a, \omega)}, \quad (1)$$

where $Z \equiv -B_r$ and $H \equiv -B_\vartheta$, a is the Earth's mean radius, ϑ is geomagnetic colatitude, ω is angular frequency, and $\mathbf{r}_a$ is geomagnetic observatory position. The responses were estimated at eight Australian geomagnetic observatories whose locations are shown in Fig. 1. For station details we refer to Table 1. The C-response estimates were obtained by Semenov & Kuvshinov (2012) who paid special attention to data selection. They used very long time-series (up to 51 yr; 1957–2007) of hourly means; these time-series were then visually inspected and data containing gaps, spikes and/or involving baseline jumps were excluded from the analysis. No attempt has been made to edit the data in order to avoid any uncertainties associated with the necessarily subjective editing schemes. A robust section-averaging approach (*cf.* Kuvshinov & Olsen 2006) was used to estimate C-responses, and jackknife estimator (*cf.* Efron 1982) was invoked to obtain trustworthy estimates of experimental errors. For further details of data analysis the reader is referred to Semenov & Kuvshinov (2012). Left- and right-hand plots in Fig. 2 show real and imaginary parts of the estimated (experimental) C-responses, respectively.

3 FORWARD AND INVERSE PROBLEMS

3.1 Forward problem and model parametrization

The geographical extent of the area modelled lies between 5°S and 55°S in latitude and 90°E and 180°E in longitude, and covers the depth range 410–1600 km. Regions outside of the investigated area are fixed horizontally and vertically to a background 1-D model (Fig. 3). This 1-D model is based on the initial model (described later). The modelled area is chosen to be wider than the actual region spanning the observatories (7.5–42.50°S, 102.5–167.50°E) in order

Table 1. List of geomagnetic observatories in Australia. Latitude and Longitude indicate a position of each geomagnetic observatory in geographical coordinates. Mag. lat. indicates a latitude in geomagnetic coordinates. Obs. period is a period to acquire geomagnetic data. Period range specifies periods at which *C*-responses were estimated.

Code	Geomagnetic obs.	Latitude	Longitude	Mag. lat.	Obs. period (yr)	Period range (d)
ASP	Alice Springs	23.8°S	133.9°E	−32.6°	1992–2007	4–100
CNB	Canberra	35.3°S	149.4°E	−42.5°	1979–2007	4–100
CTA	Charters Towers	20.1°S	146.3°E	−27.8°	1990–2007	4–70
GNA	Gnangara	31.8°S	115.9°E	−41.7°	1957 – 2007	4 – 60
KDU	Kakadu	12.7°S	132.5°E	−21.7°	1995 –2007	4–100
LRM	Learmonth	22.2°S	114.1°E	−32.1°	1990–2007	4–60
TOO	Toolangi	37.5°S	145.5°E	−45.1°	1957–1979	4–50
WAT	Watheroo	30.3°S	115.9°E	−40.2°	1957–1958	4–50

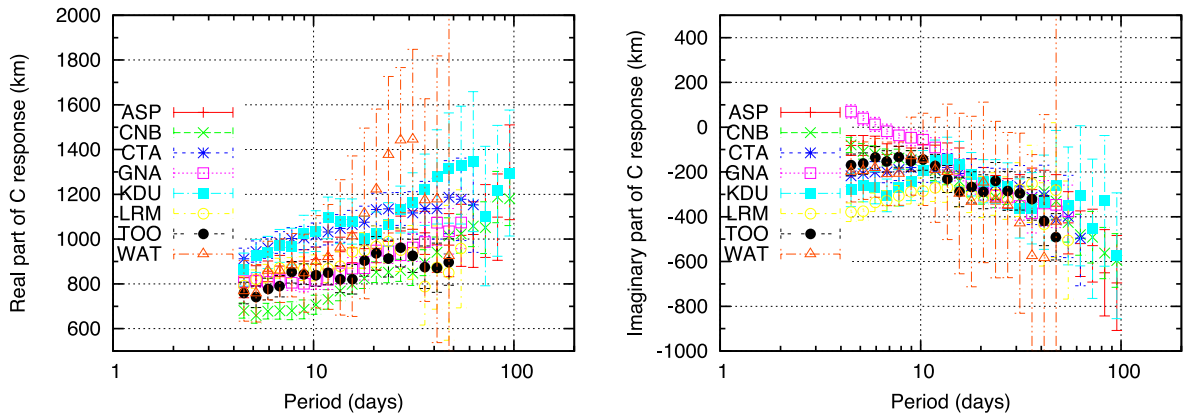

Figure 2. Plots of *C*-response data with error bars for the eight geomagnetic observatories used in this study. Real part and imaginary part of the *C*-responses are shown on the left- and right-hand side, respectively.

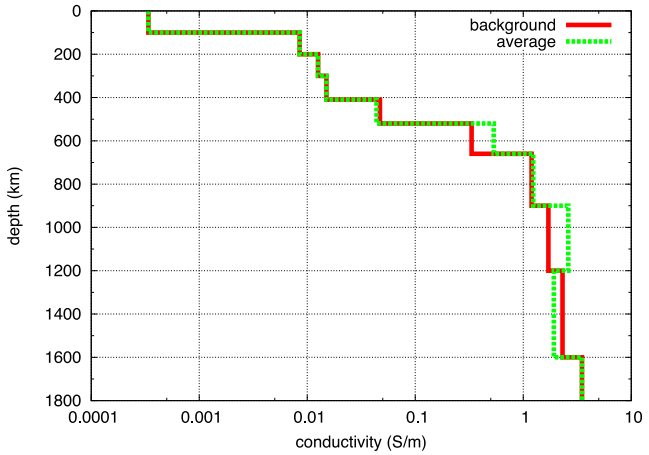

Figure 3. 1-D 'reference' models used in this study. The 'background' 1-D model is derived from averaging the initial 3-D conductivity model (see Fig. 4), while 'average' is the 1-D conductivity model obtained from averaging the recovered 3-D conductivity model (see Fig. 5). For details see main text.

to assure that the synthetic data are not affected by the conductivity structure of the surrounding (fixed) region. The horizontal cell sizes during forward and inverse modelling are $1^\circ \times 1^\circ$ and $5^\circ \times 5^\circ$, respectively. The truncation degree of the spherical harmonic expansion in our code (to calculate Green's dyad) is 80 (see Appendix A).

Lateral heterogeneities are assumed to be present in the depth range 410–1600 km. Our decision not to search for conductivity variations beyond this range is based on the fact that we interpret the *C*-responses in the period range 4–100 d, which corresponds to EM-field penetration depths ranging from about 500 to 1200 km. This inference is based on the real part of the experimental responses in a 1-D environment being proxy for penetration depth (Weidelt 1972). Given sensitivity of the data to conductivity variations outside of this range, we enlarged the target depth range to 410–1600 km. We performed trial inversions where we searched for conductivity variations in the shallow upper mantle (depths <410 km). As expected no substantial differences were observed (not shown here for brevity) in comparison to what was found for the expanded depth range.

Vertically, we parametrized the 3-D conductivity distribution using five spherical inhomogeneous layers of 110, 140, 240, 300 and 400 km thickness, resulting in conductivity boundaries at depths of 410, 520, 660, 900, 1200 and 1600 km, respectively. This division coincides with major mantle mineral phase transitions and the layering used by Kelbert *et al.* (2009) and Semenov & Kuvshinov (2012). The layers were embedded into a background 1-D section (see later).

Most of the observatories are located near the coast (see Fig. 1). As shown by Kuvshinov (2008) and Semenov & Kuvshinov (2012), for example, the *C*-responses at coastal observatories are strongly affected by a large conductivity contrast between ocean and land. To account for this effect the model includes a non-uniformly thin surface layer with laterally varying conductance, which is fixed throughout the inversion. The conductance of this layer, which is mostly governed by bathymetry, is shown in Fig. 1.

The initial (starting) 3-D model used in the inversion (see Fig. 4)—along with the background 1-D section—was constructed from a regional seismic tomography study of the Australian continent. This differs from more conventional approaches employing

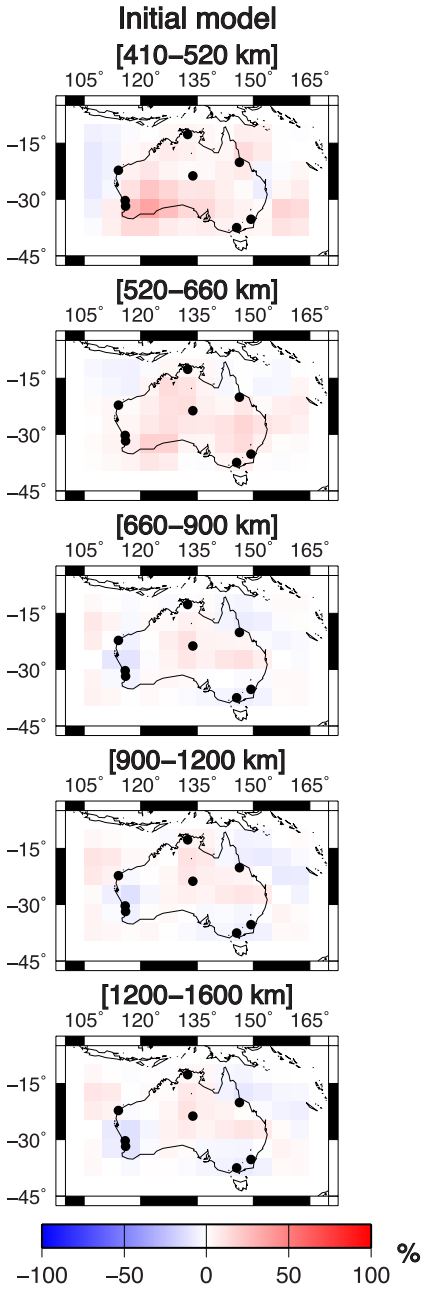

Figure 4. Initial model based on inversion of seismic surface wave data (for details see main text). The plots show variations in conductivity relative to the 1-D background model shown in Fig. 3.

1-D models that provide an average fit to data (e.g. Utada *et al.* 2003; Shimizu *et al.* 2010a). Concerning our initial model Khan *et al.* (2013) inverted surface wave phase velocities for the thermochemical structure of the mantle beneath Australia using a thermodynamic method that provides the link between thermochemical parameters and geophysical data. The thermodynamic procedure yields the amounts, compositions and physical properties, including elastic moduli, of the stable minerals in the model chemical system. To convert stable mineralogy to electrical conductivity, mineral modes are combined with laboratory electrical conductivity measurements for the relevant minerals to estimate the bulk electrical conductivity structure as described in detail in Khan & Shankland (2012). The initial conductivity model thus created bears an imprint of seismic tomography. Note that the recovered conductivity distribution covers depths from the surface of the Earth to 2000 km. By averaging the conductivity of this model horizontally at each depth node we obtained a 1-D conductivity profile (σ_{1D}), which represents our background 1-D section. This 1-D section is depicted in Fig. 3, whereas Fig. 4 shows relative variations in conductivity (in per cent) of the initial 3-D conductivity model (σ_{3D}^{init}) in the depth range 410–1600 km. Here the relative variation in conductivity $\delta\sigma$ is determined as

$$\delta\sigma(r,\theta,\phi) \equiv \frac{\sigma_{3D}^{init} - \sigma_{1D}}{\sigma_{1D}} \times 100. \quad (2)$$

Concerning the source configuration we approximate this to be in the form of an external dipole field in the geomagnetic coordinate system, which is a valid approximation in the considered period range.

3.2 Inverse problem formulation

We consider the regularized non-linear least-squares optimization problem in which we minimize the following functional $\Phi(\boldsymbol{m})$:

$$\Phi(\boldsymbol{m}) = \frac{1}{N}\sum_{i=1}^{N}\left|\frac{D_i - F_i(\boldsymbol{m})}{e_i}\right|^2 + \lambda\left|W\boldsymbol{m}\right|^2. \quad (3)$$

Here $\boldsymbol{m}$ is a set of model parameters of dimension M that we invert for (logarithm of conductivity within each cell), N is total number of data points and D_i and e_i are experimental EM responses and errors, respectively. $F_i(\boldsymbol{m})$ is the synthetic EM response of model $\boldsymbol{m}$, which is numerically calculated by 3-D forward modelling. i is a serial number of data parameters in the data set, which is related to the type of the data (real part or imaginary part of the C-response), frequency and position of geomagnetic observatory. Thus, the first term on the right-hand side (RHS) of eq. (3) is the normalized misfit. The second term is the regularization term, where λ and W are regularization parameter and smoothing matrix, respectively. The smoothing matrix W takes the form of the finite difference approximation to the horizontal gradient operator. This means that no vertical smoothing is applied. During inversion the regularization parameter λ is chosen such that the normalized data misfit is around 1.

To minimize the objective functional $\Phi(\boldsymbol{m})$ a gradient-based (quasi-Newton) method is invoked (see Appendix B for details). For efficient calculation of misfit function gradients the adjoint source approach is employed (e.g. Pankratov & Kuvshinov 2010).

To calculate synthetic C-responses and the misfit function gradient (forward problem), we employ a numerical solution based on the contracting integral-equation (CIE) approach (*cf.* Pankratov *et al.* 1995; Singer 1995). Note that there exist two independent global-based CIE-based numerical solutions (introduced by Koyama 2001 and Kuvshinov *et al.* 2002), which allow us to compute EM fields in fully 3-D conductivity models. These solutions differ in many aspects; for example, they exploit different strategies for computing the dyad Green's functions. Unfortunately, in both aforementioned analyses little attention was paid to the details of how Green's tensors (which are the cornerstone components of any integral-equation solution) are derived and calculated. Only recently did Kuvshinov & Semenov (2012) provide the necessary details for their solution. In this paper we fill this gap (see Appendix A) for the CIE-based solution of Koyama (2001). Note that this CIE solution has previously been used in a number of semi-global studies (Koyama *et al.* 2006; Utada *et al.* 2009; Shimizu *et al.* 2010b).

4 3-D INVERSION RESULTS

The final 3-D model of the mantle conductivity structure beneath the Australian continent obtained from inversion of the *C*-responses is shown in Fig. 5. Stations are unevenly distributed across the continent and we expect this to have an effect on the structural features that can be resolved. Experimental *C*-responses and the responses based on the initial and final 3-D models are shown in Fig. 6. Inspection of the response curves reveals a number of interesting features:

(i) the overall *C*-response of the initial model is good, in particular as concerns the imaginary part of the *C*-response, supporting the choice of the initial model as starting model in the inversion;

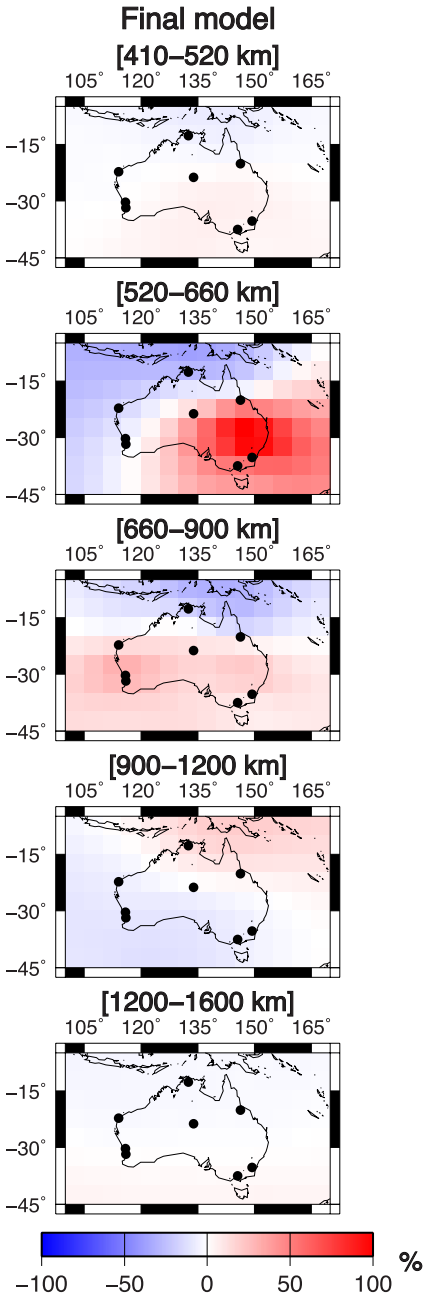

Figure 5. Final 3-D model obtained from inversion of geomagnetic observatory data. The plots show variations in conductivity relative to the 1-D background model shown in Fig. 3.

(ii) improvement in the real part of the *C*-response is achieved for stations CNB, CTA, KDU and to some extent TOO, implying that the most significant changes in conductivity are to be expected underneath these stations relative to the initial model (see Section 5 for further discussion);

(iii) as a whole, the initial model appears to be too conductive for KDU and CTA, and more resistive for CNB and TOO;

(iv) the contribution of the imaginary part of the *C*-response in determining structural features is most probably minor.

These features are supported by the conductivity maps shown in Fig. 5. The final model is clearly uniformly more resistive than the initial model in the depth range 410–520 km. The most striking changes to conductivity structure are apparently in the depth range 520–660 km, that is, in the lower part of MTZ, and, albeit to a lesser extent, in the range 660–900 km depth. In the lower MTZ we observe a strong conductivity anomaly in the southeastern part of the Australian continent reaching conductivities of $\sim$1.1 S m^{-1}, which is fairly high relative to the conductivity in the surrounding MTZ (0.3–0.6 S m^{-1}). For comparison, in a study of conductivity heterogeneities in the mantle based on a more localized approach, conductivities beneath station ASP were found to bracket the range 0.1–0.3 S m^{-1} (Khan *et al.* 2011a) at 600 km depth. Moreover, conductivities computed on the basis of laboratory data (to be discussed in more detail in Section 5) assuming a 'standard' mantle adiabat (e.g. Brown & Shankland 1981) and a uniform mantle composed of 'dry' pyrolite also lie in the range 0.1–0.3 S m^{-1}.

In the depth range 660–900 km we also observe enhanced conductivities in the southeastern part, as a continuation of the strong feature in the layer immediately above, in addition to a slightly stronger feature in the southwest. Conductivities reach values of 1.4–1.6 S m^{-1}, which are only slightly higher than the background average value at this depth of $\sim$1 S m^{-1}. In the upper part of the lower mantle, corresponding to the depth range 900–1200 km, conductivities appear more uniform and anomalies are clearly no longer present beneath 1200 km depth.

In summary, there appears to be considerable evidence for heterogeneities in conductivity in the depth range 520–900 km, particularly in the range encompassing the lower MTZ. Comparison to the global seismic shear wave tomography models SAW642AN (Panning & Romanowicz 2006) and S362ANI (Kustowski *et al.* 2008) shows that in the lower MTZ our maps generally contain more structure than is present in either SAW642AN and S362ANI. In the upper part of the lower mantle our maps, SAW642AN and S362ANI are relatively smooth down to 1600 km depth, which defines the extent to which we can presently sense. The absence of strong heterogeneities at long wavelengths below 650 km is observed in both S362ANI and SAW642AN as well as in most previous shear wave tomography studies as a transition to spectrally whiter low-amplitude mid-mantle isotropic velocity anomalies (Becker & Boschi 2002). Interpretation of these anomalies from the point of view of experimental conductivity measurements and laboratory-based conductivity profiles are discussed further in Section 5.

Finally, the good agreement of the *C*-response functions of the initial model suggests a fairly high degree of correlation or semblance between seismic velocity and electrical conductivity structure. This contrasts with current observations where comparison of 3-D conductivity anomalies (Kelbert *et al.* 2009; Kuvshinov & Semenov 2012) with 3-D shear wave velocity anomalies (e.g. in SAW642AN and S362ANI) on a global scale shows little correlation. More significantly, it reveals the strength of the thermodynamic-based approach of Khan *et al.* (2013) in being able to simultaneously

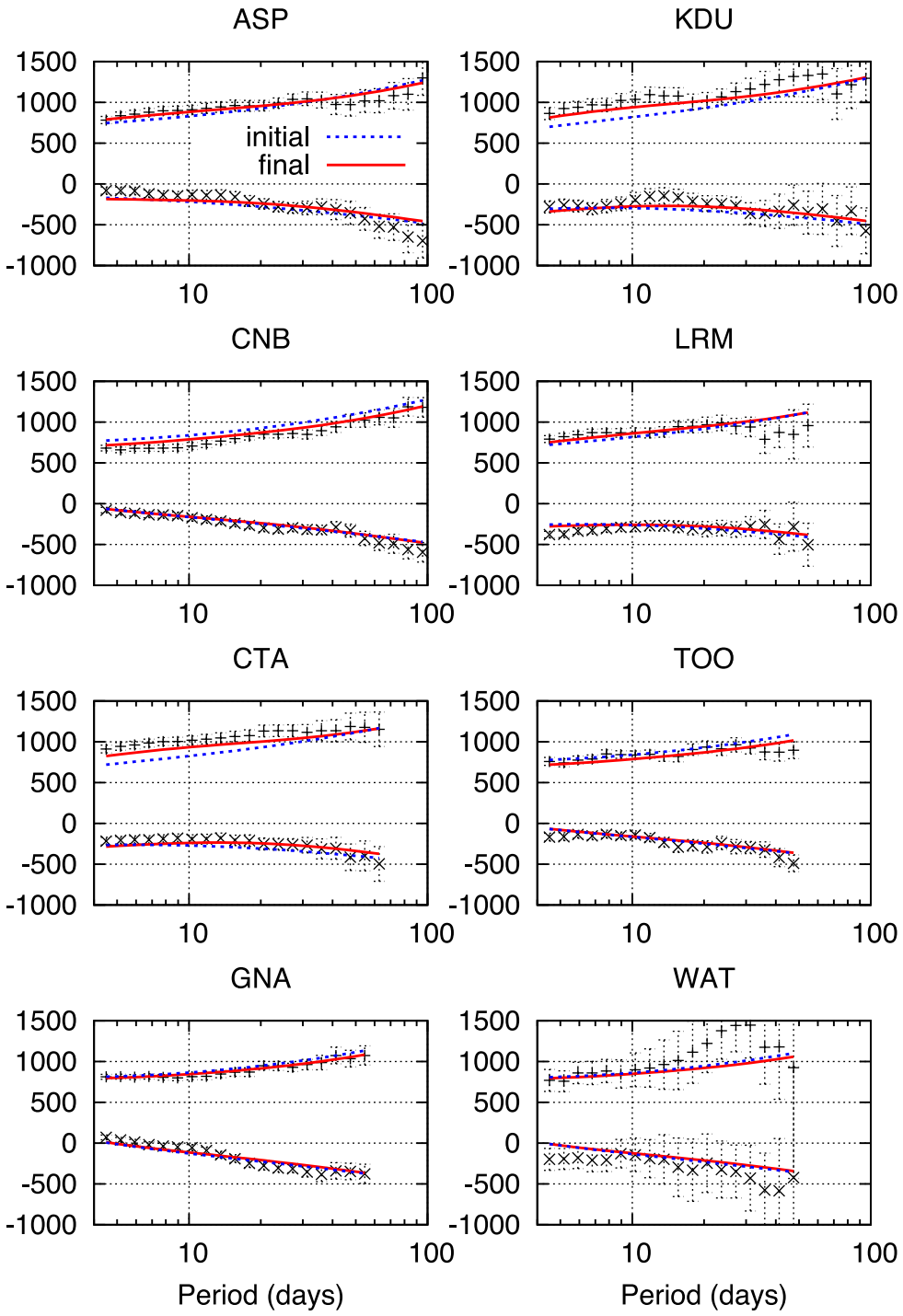

Figure 6. Comparison of computed and observed *C*-responses at the eight Australian geomagnetic observatories employed here. Experimental data are shown in black with error bars taken from Semenov & Kuvshinov (2012). Blue dotted curves and red solid curves show the synthetic data for the initial and final 3-D models, respectively. Upper and lower curves in each figure denote real and imaginary part of the *C*-responses (km), respectively.

derive conductivity and shear wave velocity models from a common thermochemical model that fits a host of different data sets.

To establish an estimate of the horizontal and vertical resolution of the model parameters we employ checkerboard tests. We use a 2-D non-uniform land/ocean surface conductance shell as topmost layer followed by five layers (either laterally homogeneous or inhomogeneous) at depths between 410 and 1600 km, embedded in a 1-D background section. Depth ranges of these five layers are as indicated previously. Five data sets are prepared. The first data set is for the 3-D model with a laterally inhomogeneous conductivity distribution located in the depth range 410–520 km, while the other layers are laterally homogeneous (fixed to 1-D background section). The conductivity structure within the inhomogeneous layer has a checkerboard pattern as shown in Fig. 7. The second data set

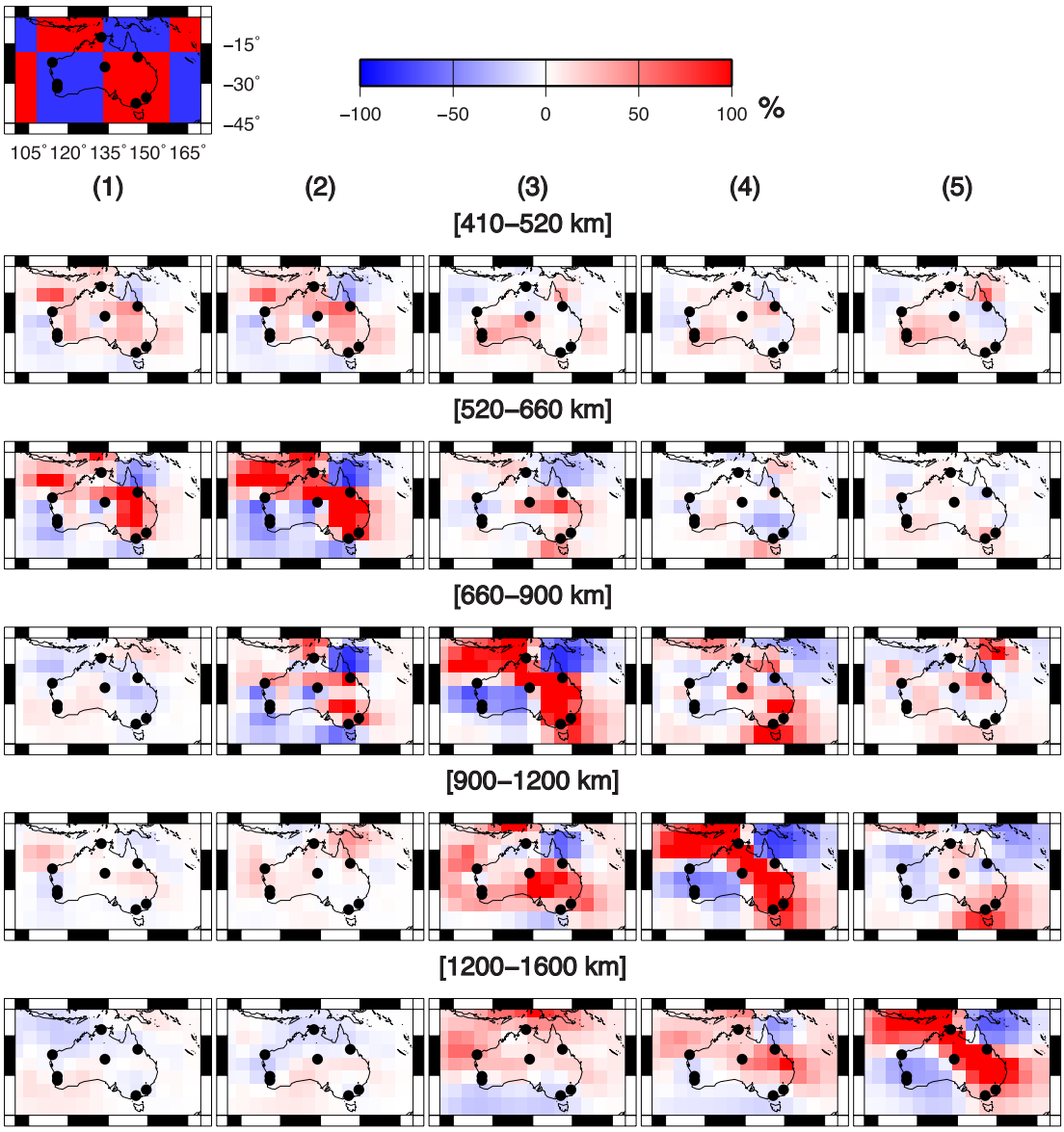

Figure 7. Resolution matrix depicting horizontal and vertical resolution of model parameters. Plot in upper left-hand corner shows true checkerboard pattern. With perfectly resolving data the 'matrix' should be in diagonal form with the true checkerboard pattern along the diagonal. For these tests no errors were added to the synthetic data or any smoothness constraints applied. See main text for details.

is for the 3-D model where the target layer containing the inhomogeneities is located in the depth range of 520–660 km, while the other layers are laterally homogeneous as before. By successively moving the target layer deeper the remaining data sets are constructed. Note that by data we consider *C*-responses at the observed observatory locations in the period range of 4–100 d. Based upon these five data sets resolution studies are performed. The results are shown in Fig. 7. The *n*-th column (from left to right) corresponds to a 3-D inversion of the *n*-th data set, with the implicit assumption that all five layers are inhomogeneous, that is, we are attempting to locate the conductivity structure in all of the layers and not only in the 'target' layer. Note that with perfectly resolving data the 'matrix' of maps in Fig. 7 should be in diagonal form with the true checkerboard pattern along the diagonal. For these tests no errors were added to the synthetic data nor were any smoothness constraints applied. Fig. 7 demonstrates that the recovered pattern appears reasonably well resolved in the depth range 520–1600 km, although the anomaly appears to 'leak' into neighbouring layers. These resolution studies imply that with current data we are able to image the conductivity distribution reasonably in the depth range of 520–1600 km.

We also performed an additional series of tests, that is, inversions, with the purpose of establishing the robustness of our obtained results, in particular the strong MTZ conductivity anomaly observed beneath the southeastern part of the continent. We considered the effects of differing (1) parametrization of the inverse problem, (2) discretization of the forward problem, (3) amount of data both with respect to period and number of observatories and (4) level of regularization. Remarkably enough most of the results (not shown here for brevity) support the presence of a region with elevated conductivity in the lower MTZ and upper part of the lower mantle beneath southeastern Australia.

5 INTERPRETATION OF CONDUCTIVITY ANOMALIES AND IMPLICATIONS FOR TRANSITION-ZONE THERMAL STRUCTURE, WATER CONTENT AND MELTING

5.1 Preliminaries

In this section, we attempt to draw inferences about the underlying processes that produce the mantle conductivity anomalies found here. For this purpose we rely on experimental measurements of mantle mineral conductivities and combine these with mantle mineral phase equilibrium computations at the pressure–temperature conditions of interest to obtain what we shall term laboratory-based conductivity profiles. To compute phase equilibria we employ the Gibbs free-energy minimization method of Connolly (2005), which predicts, for a given pressure, temperature and composition (we employ the CMFASNa model system comprising the oxides of elements CaO-MgO-FeO-Al_2O_3-SiO_2-Na_2O), stable mineralogy (mineral modes) and physical properties (e.g. *P*-, *S*-wave speed, and density). We specifically investigate the variation of the constructed laboratory-based conductivity profiles with temperature, major element composition and water content and in this manner determine the controlling factors needed for such profiles to fit the inverted conductivity models. The approach is described in detail in, for example, Khan *et al.* (2006) and, more recently, in Khan & Shankland (2012). For brevity this section only summarizes the method; for details we refer the reader to the earlier studies.

To facilitate comparison with other models we have extracted 1-D conductivity profiles from our final conductivity model along a specific latitude (27.5° S) and longitude (107.5–152.5° E in 5° steps). These 1-D profiles are shown in Fig. 8 and are compared to a series of geophysically derived global 1-D models that include the global models of Kuvshinov & Olsen (2006), Velimsky (2010), the subcontinental European model of Olsen (1999) and the laboratory-based models of Xu *et al.* (2000) and Khan *et al.* (2006). Relative to the presently inverted profiles, the geophysically derived 1-D models are typically too conductive in the upper and too resistive in the lower part of the MTZ, thereby emphasizing the anomalous nature of this part of the mantle beneath Australia. Moreover, purely geophysically derived models are characterized by a continuous conductivity increase across the MTZ, whereas the profiles obtained here, like previous laboratory-based models, implicitly incorporate discontinuities across major phase transitions (the '410-km', '520-km' and '660-km' seismic discontinuities). These phase transitions correspond to locations where the transformations olivine→wadsleyite (410), wadsleyite→ringwoodite (520) and ringwoodite→ferriperoclase+perovskite (660) occur, respectively.

The most striking feature of the model presented here is the high-conductivity anomaly in the lower part of the MTZ (520–660 km depth) beneath southeastern Australia. The high-conductivity region is 0.5–1 log unit more conductive than the other models shown in Fig. 8 and clearly points to strong compositional (major elements, water content) and/or thermal anomalies. Water likely plays a prominent role because transition-zone (TZ) minerals wadsleyite and ringwoodite can support high water contents (e.g. Smyth 1987; Inoue *et al.* 1995; Chen *et al.* 2002) and electrical conductivity is known to be highly sensitive to presence of water (e.g. Karato 1990). Recent experiments on wadsleyite and ringwoodite

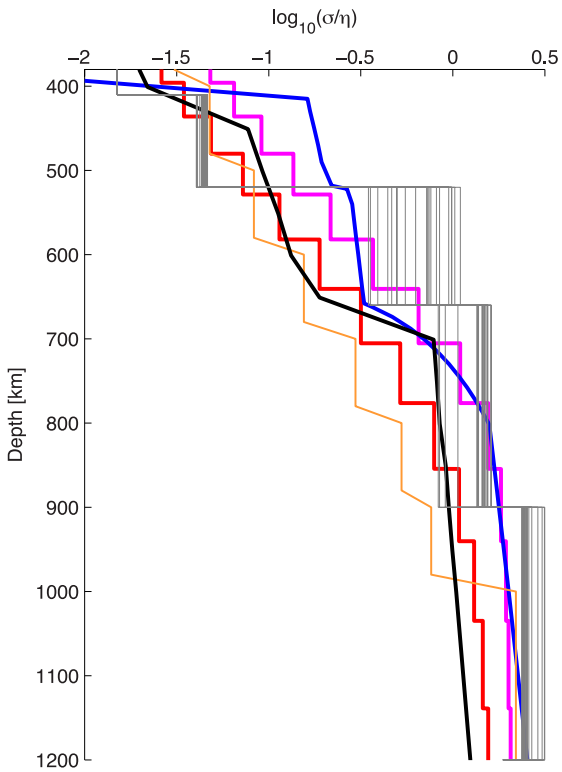

Figure 8. Summary of radial and 1-D global and regional conductivity profiles. Thin grey lines depict radial conductivity profiles ('observed' profiles) extracted from the inverted model (Fig. 5) beneath 10 equally spaced grid points along a specific latitude (27.5° S). For comparison, a series of laboratory-based conductivity models are also shown: Xu *et al.* (2000, blue) and Khan *et al.* (2006, black), in addition to the purely geophysically derived models of Olsen (1999, red), Kuvshinov & Olsen (2006, magenta) and Velimsky (2010, orange). Note that the model by Khan *et al.* (2006) is the mean profile, and uncertainties (not shown) are typically of the order of $\pm 0.5\ \mathrm{S\,m^{-1}}$. $\eta = 1\ \mathrm{S\,m^{-1}}$.

have confirmed the sensitivity of electrical conductivity to water content, although discrepant measurements have resulted in a controversy that is yet to be resolved (see e.g. summaries by Karato 2011; Yoshino & Katsura 2012, 2013).

Data from both groups were considered separately by Khan & Shankland (2012) to infer mantle water content from a quantitative analysis of EM sounding data. Here, we continue with the data compiled in Khan & Shankland (2012) but limit ourselves for reasons of brevity and ease of use to the measurements by Yoshino, Katsura and coworkers (hereinafter referred to as YK) for the hydrous minerals olivine, orthopyroxene, wadsleyite and ringwoodite. Relative to Khan & Shankland (2012) we have updated and expanded the conductivity database to include recent measurements. The conductivity data are summarized in Fig. 9 and are taken from Yoshino *et al.* (2009) and Yoshino *et al.* (2012b) for olivine (ol), from Zhang *et al.* (2012) for orthopyroxene (opx), from Xu & Shankland (1999) for clinopyroxene (cpx), from Yoshino *et al.* (2008b) for garnet (gt), from Yoshino & Katsura (2012) for wadsleyite (wads), from Yoshino *et al.* (2008a), Yoshino & Katsura (2009) and Yoshino *et al.* (2012b) for ringwoodite (ring), from Katsura *et al.* (2007) for akimotoite (aki), from Xu *et al.* (2000) for ferropericlase (fp) and from Xu *et al.* (1998) for perovskite (pv).

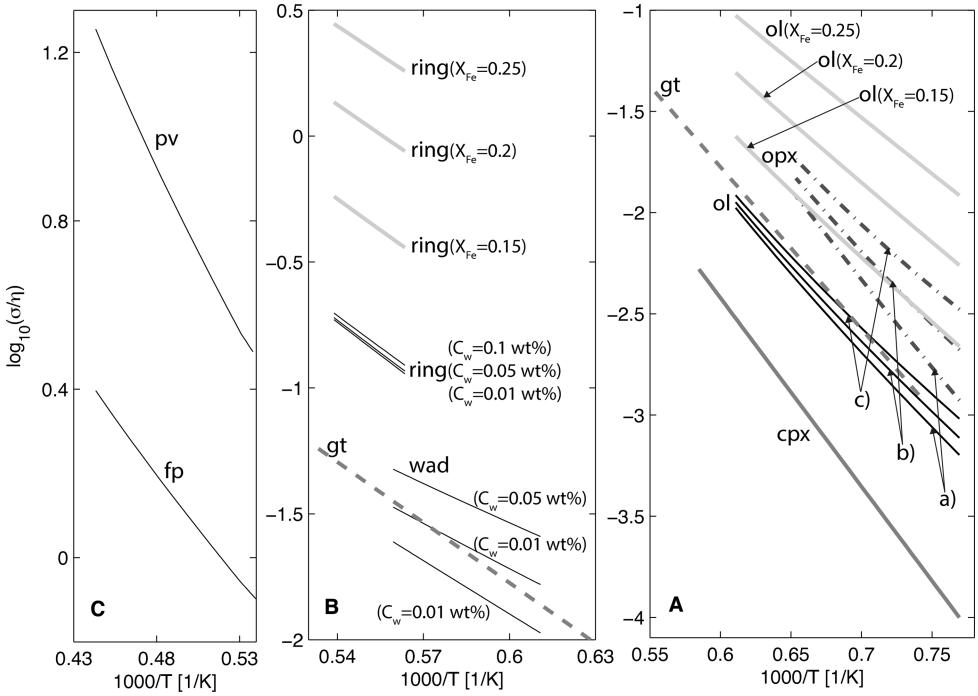

Figure 9. Summary of electrical conductivities measured in the laboratory as a function of inverse temperature for major upper-mantle, transition-zone and lower-mantle minerals. Phases are ol (olivine), opx (orthopyroxene), cpx (clinopyroxene), C2/c (high-pressure Mg-rich Cpx), gt (garnet), wads (wadsleyite), ring (ringwoodite), aki (akimotoite), ca-pv (calcium perovskite), fp (ferropericlase), pv (perovskite) and CF (calcium ferrite). Plot A depicts upper-mantle single mineral conductivities. For phases ol and opx, conductivity also varies with H_2O and Fe content (X_{Fe}, ol only). Lines labelled (a), (b) and (c) correspond to 0.001, 0.005 and 0.01 wt per cent H_2O, respectively, with X_{Fe}^{ol} fixed to 0.1. Plot B shows conductivity variations for transition-zone minerals gt, wads and ring. For wads and ring, conductivity also varies with H_2O (C_w) and Fe content (X_{Fe}, ring only). Plot C shows conductivities of lower mantle minerals pv and fp. Stability field of each mineral is computed based on the assumption of a fixed pyrolitic bulk composition and a standard mantle adiabat as depicted in Fig. 10 below. See main text for further discussion. $\eta = 1\ \mathrm{S\,m^{-1}}$.

5.2 Conductivity data and laboratory-based conductivity profiles

In order to make quantitative inferences of the observed MTZ conductivity anomalies we construct laboratory-based conductivity profiles by combining laboratory data with a self-consistently computed mineralogical model of the Earth's mantle using Gibbs free energy minimization (Connolly 2005). For purposes of illustration, we assume a chemically homogeneous and adiabatic mantle using the geotherm of Brown & Shankland (1981). Resulting phase equilibria (equilibrium mineralogy) computed on this basis are shown in Fig. 10. Bulk electrical conductivity as a function of pressure, water and Fe content for this particular mineral assemblage is obtained by combining the mineral phase proportions with the laboratory-measured mineral conductivities (Fig. 9) at the appropriate physical conditions (temperature and pressure) and composition of interest. Computing bulk rock electrical conductivity from single mineral conductivities is done by averaging the contribution from individual minerals, for which purpose we employ effective medium theory (Landauer 1952; Berryman 1995) to produce a self-consistent solution. This and other averaging schemes for constructing bulk rock conductivity are discussed further in Khan & Shankland (2012) and Xu *et al.* (2000).

Factors that potentially contribute, but that we neglect here, include oxygen fugacity (f_{O_2}), defect chemistry (e.g. Al), grain boundary transport, effects of pressure and minor mineral phases as their contributions are expected to be relatively unimportant (e.g. Karato 2011; Dai *et al.* 2012; Khan & Shankland 2012). Effects of water on mineral phase equilibria are also disregarded here. Although there is evidence from theory (e.g. Wood 1995) and experiment (e.g. Chen *et al.* 2002; Smyth & Frost 2002; Litasov *et al.* 2006) that water is likely to stabilize wadsleyite over olivine, scarcity of relevant thermodynamic data prevents us from including this effect. However, given that the water-induced conductivity change across the olivine→wadsleyite transition is relatively small (*cf.* Fig. 10), this issue is of minor importance. Finally, no exhaustive attempt was made to consider other conductivity compilations (e.g. Vacher & Verhoeven 2007; Pommier & Trong 2010; Jones *et al.* 2012).

The laboratory-based conductivity profiles shown in Fig. 10 contain discontinuities in conductivity at the location of major mineralogical phase transitions where (1) olivine transforms to wadsleyite (∼14 GPa), (2) wadsleyite transforms to ringwoodite (∼21 GPa) and (3) ringwoodite transforms to ferriperoclase and perovskite (∼23.5 GPa). As expected, magnitudes of the various transitions are observed to depend strongly on water and Fe content.

5.3 Inverse analysis

To treat the problem somewhat more quantitatively than is possible by simple comparison of the 'observed' 1-D profiles shown in Fig. 8 with various laboratory-based profiles computed for different water contents, geotherms and mantle compositions, we consider interpretation of the observed profiles as an inverse problem, that is, we invert the 'observed' 1-D profiles (Fig. 8) for mantle temperature, water content and major element composition using the thermodynamic approach described earlier. From this quantitative approach we gain a more comprehensive understanding of the effects and trade-offs of the various parameters.

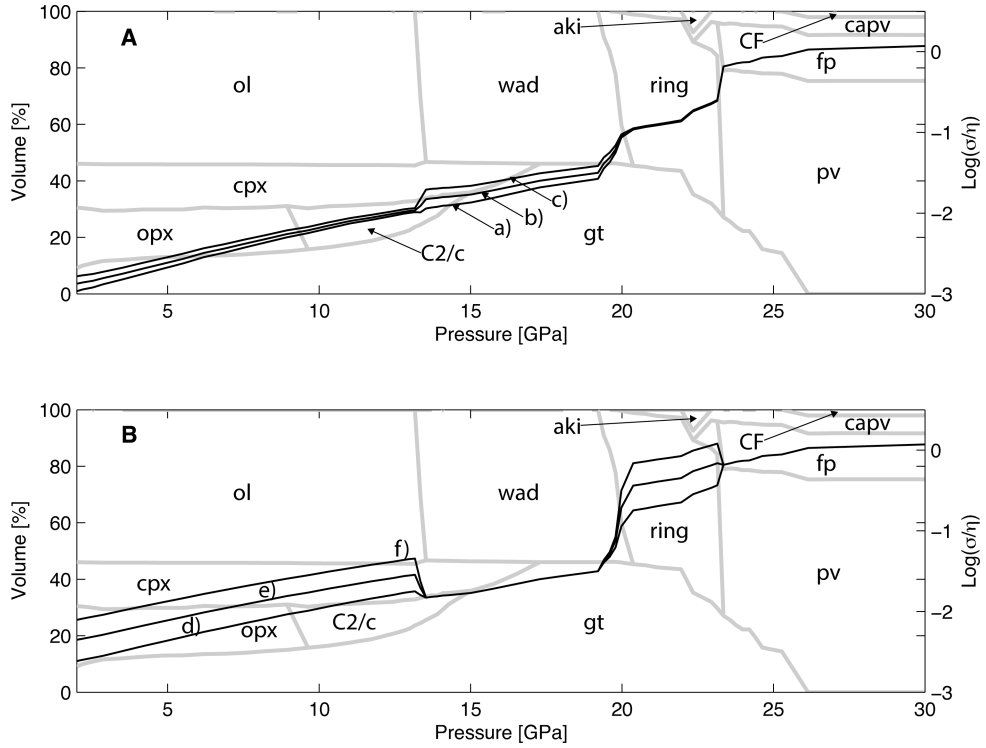

Figure 10. Modal mineralogy and associated laboratory-based bulk electrical conductivity profiles as a function of pressure for various water (A) and Fe contents (B). Phase proportions and bulk conductivity profiles are computed on the basis of a homogeneous adiabatic pyrolitic mantle. Lines labelled (a), (b) and (c) in plot A depict bulk conductivity profiles for water contents (C_w) of 0.001/0.005/0.01 wt per cent (ol, opx) and 0.01/0.05/0.1 wt per cent (wad, ring), respectively, with Fe content (X_{Fe}) fixed to 0.1. Lines labelled (d), (e) and (f) in plot B show bulk conductivity profiles for $X_{Fe} = 0.15$, 0.2 and 0.25, respectively. For these profiles we fixed $C_w^{ol/opx} = 0.005$ and $C_w^{wad/ring} = 0.05$. Fe-dependent conductivity has only been measured for minerals ol and ring. See main text for further discussion. $\eta = 1\ S\,m^{-1}$.

For this purpose we employ a Markov chain Monte Carlo (McMC) method (e.g. Mosegaard & Tarantola 1995) to sample the model parameter space, that is, produce a set of samples of the various parameters involved (mantle water content, geotherm and composition) that constitute the solution to the inverse problem. All samples from the model space fit data within uncertainties. In the present context data are in the form of an average 'observed' 1-D conductivity profile that we attempt to fit to within an uncertainty of 25 per cent in order that the whole range of 1-D conductivity profiles shown in Fig. 8 is encompassed.

The various parameters are varied within certain (prior) ranges: water content in olivine, orthopyroxene, wadsleyite and ringwoodite varies log-uniformly in the ranges $\log_{10}(C_w^{ol}/C_w^0) \in [-5;-1]$, $\log_{10}(C_w^{opx}/C_w^0) \in [-5;-1]$, $\log_{10}(C_w^{wad}/C_w^0) \in [-5;-0.3]$ and $\log_{10}(C_w^{ring}/C_w^0) \in [-5;-0.3]$, respectively, where C_w is water content in wt per cent and C_w^0 is reference water content (1 wt per cent). Prior constraints on mantle geotherm derive from petrological experiments on mineral phase transitions in the system $(Mg,Fe)_2SiO_4$. Ito & Takahashi (1989) found that the olivine→wadsleyite ('410-km') and ringwoodite→ferriperoclase+perovskite ('660-km') reactions occurred at temperatures of 1750 ± 100 K and 1900 ± 150 K, respectively, in line with the results of Katsura *et al.* (2010) who derived temperatures of 1830 ± 50 K and 1990 ± 50 K, respectively, for the same reactions. In line with this, lower and upper bounds apply at depths where the transformations olivine→wadsleyite (1470–1640 °C) and ringwoodite→fp+pv (1650–1800 °C) occur. No further bounds apply to the geotherm, except for that of a non-decreasing temperature profile with depth. Major element composition is varied within the range of model estimates of the primitive upper-mantle composition compiled by Lyubetskaya & Korenaga (2007).

Mantle water content has to be seen in relation to water storage capacities of mantle minerals. Water storage capacity is the maximum amount of water that a mineral or rock at a given pressure and temperature is able to retain without producing a hydrous fluid (water- or silicate-rich). The importance of storage capacity arises because different minerals have different storage capacities, which in turn limits potential reservoirs. For wadsleyite, for example, an upper bound of ∼3 wt per cent has been measured (e.g. Inoue *et al.* 1995; Kohlstedt *et al.* 1996; Bolfan-Casanova *et al.* 2000; Chen *et al.* 2002). This maximum estimate for wadsleyite, however, is too high given that Demouchy *et al.* (2005) and, more recently, Litasov *et al.* (2011) showed that water solubility of wadsleyite decreases with increasing temperature providing an additional upper limit on the amount of water that can be stored in the transition zone. Litasov *et al.* (2011) found that wadsleyite at conditions relevant to the transition-zone (13–20 GPa and 1500–1600 °C) contains in the range 0.37–0.55 wt per cent H_2O. Combined with the recently determined partition coefficient of Inoue *et al.* (2010) water storage capacities around 0.15–0.3 wt per cent for ringwoodite can be inferred. For present purposes we employ a storage capacity value of 0.4 wt per cent H_2O for TZ minerals. At locations where this value is exceeded hydrous melting ensues (e.g. Kohlstedt *et al.* 1996). As a result we reparametrized our model with a melt layer appearing in the depth range 550–570 km (depth of transformation of wadsleyite→ringwoodite) if $C_w^{ring} > 0.4$ wt per cent. Given that we cannot model melt composition, we followed our previous approach (Khan & Shankland 2012) and parametrized melt

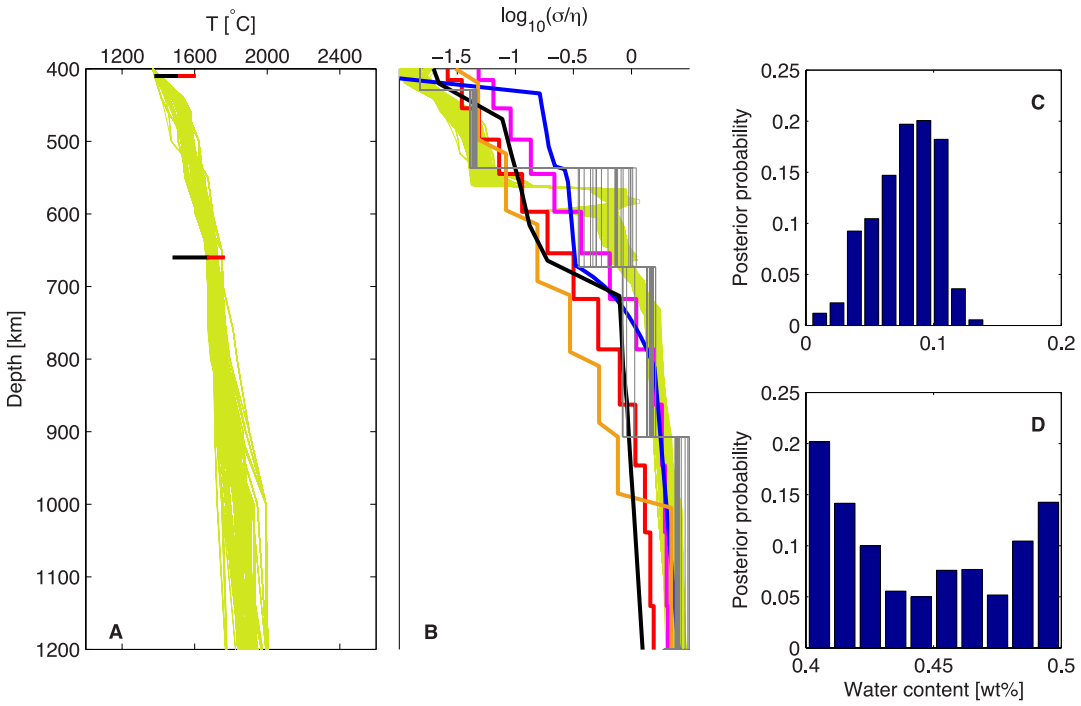

Figure 11. Sampled geotherms (A), laboratory-based conductivity profiles (B), and water content in transition-zone minerals wadsleyite (C) and ringwoodite (D) obtained by inversion of 'observed' profiles shown in Fig. 8. Solid vertical bars indicate experimentally determined temperatures for the major mineral phase reactions at 410 and 660 km depth [black bars—Ito & Takahashi (1989); red bars—Katsura *et al.* (2010). See main text for details.

conductivity according to $\sigma_{\rm melt} = \sigma_{\rm m} + \sigma' \cdot \alpha$, where $\sigma_{\rm m}$ is 'current' mantle conductivity, σ' is a constant conductivity value (5 S m^{-1}) based on available melt conductivity measurements (e.g. Pommier *et al.* 2010) and α is a random number in the interval 0–1.

By varying the parameters within these ranges the prior is updated by considering data and physical theory to the posterior via Bayes theorem (e.g. Mosegaard & Tarantola 1995). The posterior so obtained constitutes the result to the inverse problem and in the following we show samples from this posterior distribution. For further details on solving the inverse problem in the current setting the reader is referred to Khan & Shankland (2012).

5.4 Results

Sampled conductivity profiles, mantle geotherms and MTZ water content are shown in Fig. 11. Observed conductivity profiles appear to be explainable with mantle geotherms that concur with the adiabatic mantle temperatures of Katsura *et al.* (2010) at the '410-km' and '660-km' discontinuities. Water content is seen to differ between major MTZ minerals. For wadsleyite we find that $C_{\rm w}^{\rm wads}$ ranges from ∼0.05 wt per cent to 0.15 wt per cent, while for ringwoodite $C_{\rm w}^{\rm ring}$ lies in the range 0.4–0.5 wt per cent. Comparison of inverted and observed conductivity profiles provides an explanation for these ranges. $C_{\rm w}^{\rm wads}$ remains well below upper MTZ storage capacity in order that laboratory-based conductivities do not exceed the observed profiles; addition of more water would tend to increase conductivities beyond that of the observations, whereas $C_{\rm w}^{\rm ring} < 0.05$ has the opposite effect of decreasing conductivities too much. In the lower part of the TZ storage capacity (0.4 wt per cent) is clearly exceeded, which results from the inability of hydrous ringwoodite alone to explain the strong conductivity anomalies. Larger values of $C_{\rm w}^{\rm ring}$ are required that result in dehydration melting and conductivities around 1 S m^{-1} in this part of the mantle. For comparison, conductivities of various hydrous basaltic and silicate melts are in the range 0.5–2 S m^{-1} at pressures and temperatures of 2 GPa and 1673 K (e.g. Pommier *et al.* 2010).

Overall, our inverted MTZ water content is similar to inferences made by Karato (2011) and Yoshino & Katsura (2013). However, considering the simplicity of the constructed laboratory-based model and the purely qualitative model comparison made by both Karato (2011) and Yoshino & Katsura (2013), their inferred mantle water content is likely less robust. Prior compositional ranges are relatively small in line with mantle sample-based (Lyubetskaya & Korenaga 2007) estimates and compositional variations will not be discussed further here.

At this stage we neglect the dynamical fate of this melt given its unknown composition, although it might be surmised that, if less dense than surrounding mantle, it could possibly rise through the MTZ and pond on top of the 410-km seismic discontinuity for which geophysical evidence is accumulating (e.g. Song & Helmberger 2004; Toffelmier & Tyburczy 2007; Tauzin *et al.* 2010; Khan & Shankland 2012). A possibility for maintaining the hydrous nature of the MTZ relative to upper and lower mantle is through the production of melts at the bottom of the upper-mantle concomitantly with water exsolution beneath 660 km as envisaged in the water filter hypothesis (Bercovici & Karato 2003).

An alternative explanation for the large conductivity anomalies might be found in recent work on carbonatite melts. Based on the initial suggestion by Gaillard *et al.* (2008) and expanded work by Yoshino *et al.* (2012a), small amounts of carbonatite melts (∼0.1 vol per cent) are found to increase conductivity significantly beyond that possible with hydrous olivine. This, it has been argued, could account for some regional asthenospheric conductivity anomalies that hydrous olivine alone is incapable of explaining. As discussed in more detail by, for example, Litasov (2011) melting in CO_2-containing systems can also result in the presence of carbonate

melts in the MTZ. In turn, such highly conductive melts could provide an explanation for the strong conductivity anomalies that we observe here in the mid-TZ. We leave it for future studies to consider this in more detail.

An inherent problem with the analysis of conductivity data as a means of constraining mantle water content is the trade-off that is likely to occur between the various parameters sought. To test the robustness of the results obtained here we performed several additional inversions where we successively fixed one set of parameters and inverted for the remainder. For example, we considered a completely dry mantle, that is, we fixed $C_w = 0$ wt per cent for all minerals, and found that data could no longer be adequately fit. This result strongly supports arguments here and elsewhere for the presence of water in the MTZ. We also considered the case where no mid-TZ melting occured, which resulted in profiles lacking the strong conductivity anomaly of the 'observed' profiles. Generally, these miscellaneous inversions showed that considering extraneous information, where available, to independently constrain C_w and geotherm is preferable in order that trade-offs are reduced.

In summary, the inversions conducted here imply that MTZ minerals require presence of water for the observed conductivity anomalies to be adequately fit. Thus, the observed heterogeneities in the MTZ (Fig. 5) appear to be due to concomitant lateral variations in water content, thermal structure and most probably melt. The variations across the MTZ appear to span the range from (1) relatively water-poor to somewhat water-enriched minerals, (2) thermal anomalies that vary laterally by 150 °C but remain within adiabatic limits and (3) areas with and without melt. Comparison of 'observed' and inverted 1-D profiles showed that the conductivity in the mid-TZ based on hydrous wadsleyite and ringwoodite (including variations in Fe content) only is insufficient to explain the most conductive anomalies. This supports the case for dehydration melting in the MTZ and implies lateral variations in melt content that, if interconnected, very likely contribute a significant proportion to the observed conductivity (e.g. Shankland & Waff 1977; Roberts & Tyburczy 1999; Park & Ducea 2003; Pommier *et al.* 2010). We leave it for a future study to consider this in more detail. Other sources such as compositional variations in the MTZ can also be important. Although much diminished relative to those in the upper-mantle compositional variations in the MTZ are expected based on evidence provided by seismic tomography studies (e.g. Khan *et al.* 2013).

6 CONCLUSION

In this study we have inverted geomagnetic observatory data in the form of *C*-responses from eight observatories distributed across the Australian continent for the 3-D mantle conductivity structure. The *C*-response data were investigated in the period range 4–100 d, which corresponds to sensitivity in the depth range 410–1600 km. The inverted model revealed the presence of a strong conductivity anomaly in the depth range 520–900 km, most notably in the lower part of the MTZ (520–670 km depth) beneath the southeastern part of the continent. The imaged conductivity distributions clearly show considerable lateral as radial variations, which become less pronounced at mid-mantle depths.

Checkerboard tests were performed to test vertical and horizontal resolution and data sensitivity. These tests showed that data could resolve structural features in the depth range ∼500–1600 km, with highest resolution occurring in the layers corresponding to the lower part of the MTZ and uppermost lower mantle. Additional tests were undertaken to establish the robustness of the inverted model. These tests generally confirmed the features of the inverted model, in particular the conductivity anomaly in the lower part of the MTZ underneath southeastern Australia.

In a subsequent analysis we investigated the recovered conductivity distributions for implications of thermochemical structure, transition-zone water content and possible distribution of melt using experimental conductivity measurements and laboratory-based conductivity profiles. This analysis strongly suggested that the distinct transition-zone conductivity anomaly not only reflects large lateral variations in temperature and water content, but likely also in the amount of melt. Slab stagnation underneath Australia could possibly lead to locally enhanced regions of accumulated water that might exceed the water storage capacity of the major transition-zone minerals and thereby induce partial melting. Concerning the total potential reservoir of water in the transition-zone our results when extrapolated globally imply an equivalent of one to three times that of the current oceans.

Future studies using improved and complementary EM sounding data in addition to novel experimental measurements of the conductivity of hydrous lower-mantle minerals will have to investigate the findings presented here further. The lower-mantle water content is believed to be low on account of the low solubility of water in lower-mantle minerals magnesium silicate perovskite and ferropericlase (e.g. Bolfan-Casanova *et al.* 2006), and appears not to exceed 0.2 wt per cent, although this value remains debated. Moreover, the effect of water on the conductivity of perovskite and ferropericlase remains to be measured. The use of short-period EM sounding data related to S_q variations holds the potential of providing significant improvement particularly as concerns upper-mantle conductivity structure, which is not sensed by the *C*-responses investigated here (e.g. Koch & Kuvshinov 2013). Also, to improve lateral resolution the application of these techniques to relatively dense geomagnetic station arrays such as the Australia-wide Array of Geomagnetic stations (AWAGS; Chamalaun & Barton 1993) will prove important (Koch & Kuvshinov 2013).

ACKNOWLEDGEMENTS

We are grateful to the Jakub Velimsky and two anonymous reviewers for comments that improved the manuscript. We thank Hisashi Utada and Hisayoshi Shimizu for discussions concerning numerical aspects of the computations performed here. Comments by Tom Shankland and Masahiro Ichiki were also much appreciated. We would like to extend our gratitude to Jakub Velimsky and two anonymous reviewers for their comments to improve the manuscript. TK was supported by ETH during his one year stay in Zurich as an academic guest for which he would like to thank members of the institute for their hospitality. A. Khan was partly supported by Swiss National Science Foundation grant 200021-130411. Numerical computations were performed on the ETH cluster Brutus and in part on the Earth Simulator in JAMSTEC.

REFERENCES

Avdeev, D.B. & Avdeeva, A., 2009. 3D magnetotelluric inversion using a limited-memory quasi-newton optimization, *Geophysics,* **74**(3), 45–57.

Avdeev, D.B. & Knizhnik, S., 2009. 3D integral equation modeling with a linear dependence on dimensions, *Geophysics,* **74**(5), F89–F94.

Backus, G., 1986. Poloidal and toroidal fields in geomagnetic field modeling, *Rev. Geophys.,* **34,** 75–109.

Banks, R.J., 1969. Geomagnetic variations and the electrical conductivity of the upper mantle, *Geophys. J. R. astr. Soc.,* **17,** 457–487.

Becker, T.W. & Boschi, L., 2002. A comparison of tomographic and geodynamic mantle models, *Geochem. Geophys. Geosyst.,* **3,** doi:10.1029/2001GC000168.

Bercovici, D. & Karato, S.-I., 2003. Whole-mantle convection and the transition-zone water filter, *Nature,* **425,** 39–44.

Berryman, J., 1995. Mixture of rock properties: rock physics and phase relations, in *A Handbook of Physical Constants: American Geophysical Union Reference Shelf 3,* pp. 205–208, ed. Ahrens, T.J., American Geophysical Union.

Bolfan-Casanova, N., Keppler, H. & Rubie, D.C., 2000. Water partitioning between nominally anhydrous minerals in the MgO-SiO_2-H_2 O system up to 24 GPa: implications for the distribution of water in the Earth's mantle, *Earth planet. Sci. Lett.,* **193**(3–4), 501–508.

Bolfan-Casanova, N., McCammon, C.A. & Mackwell, S.J., 2006. Water in transition zone and lower mantle minerals, in *Earth's Deep Water Cycle, Geophysical Monograph Series, .* **168,** eds Jacobsen, S.D. & van der Lee, S., American Geophysical Union.

Brown, J.M. & Shankland, T.J., 1981. Thermodynamic parameters in the earth as determined from seismic profiles, *Geophys. J. Int.,* **66,** 579–596.

Broyden, C.G., Dennis, J.E. Jr & More, J.J., 1973. On the local and superlinear convergence of quasi-Newton methods, *J. Inst. Math. Appl.,* **12,** 223–245.

Campbell, W.H., Barton, C.E., Chamalaun, F.H. & Welsch, W., 1998. Quiet-day ionospheric currents and their application to upper mantle conductivity in Australia, *Earth Planets Space,* **50,** 347–360.

Chamalaun, F.H. & Barton, C., 1993. The large-scale electrical conductivity structure of Australia, *J. Geomagn. Geoelectr.,* **45,** 1209–1212.

Chen, J., Inoue, T., Yurimoto, H. & Weidner, D.J., 2002. Effect of water on olivine-wadsleyite phase boundary in the $(Mg,Fe)_2$ SiO_4 system, *Geophys. Res. Lett.,* **29**(18), doi:1.1029/2001GL014429.

Connolly, J.A.D., 2005. Computation of phase equilibria by linear programming: a tool for geodynamic modeling and an application to subduction zone decarbonation, *Earth planet. Sci. Lett.,* **236,** 524–541.

Dai, L., Li, H., Hu, H., Shan, S., Jiang, J. & Hui, K., 2012. The effect of chemical composition and oxygen fugacity on the electrical conductivity of dry and hydrous garnet at high temperatures and pressures, *Contrib. Mineral. Petrol.,* **163,** 689–700.

Demouchy, S., Deloule, E., Frost, D.J. & Keppler, H., 2005. Temperature and pressure dependence of water solubility in iron free-wadsleyite, *Am. Mineral.,* **90,** 1084–1091.

Efron, B., 1982. *The Jackknife, the Bootstrap, and Other Resampling Plans,* Society for Industrial and Applied Mathematics.

Fletcher, R., 1970. A new approach to variable metric algorithms, *Comput. J.,* **13,** 317–322.

Frost, D.J. & McCammon, C.A., 2008. The redox state of Earth's mantle, *Ann. Rev. Earth planet Sci.,* **36,** doi:10.1146/annurev.earth.36.031207.124322.

Gaillard, F., Malki, M., Iacono-Marziano, G., Pichavant, M. & Scaillet, B., 2008. Carbonatite melts and electrical conductivity in the asthenosphere, *Science,* **322**(5906), 1363–1365.

Heinson, G. & White, A., 2005. Electrical resistivity of the Northern Australian lithosphere: crustal anisotropy or mantle heterogeneity? *Earth planet. Sci. Lett.,* **232,** 157–170.

Helffrich, G.R. & Wood, B.J., 2001. The Earth's mantle, *Nature,* **412,** 501–507.

Ichiki, M., Fuji-ta, K., Wang, L., Whatman, J. & Hichman, A., 2012. A reference electrical conductivity model of continental upper mantle estimated from MT data in central Australia, in *21st EM Induction Workshop Darwin,* Extended Abstract and Poster.

Inoue, T., Yurimoto, H. & Kudoh, Y., 1995. Hydrous modified spinel, $Mg_{1.75}$ $SiH_{0.5}$ O_4: a new water reservoir in the mantle transition region, *Geophys. Res. Lett.,* **22**(2), 117–120.

Inoue, T., Wada, T., Sasaki, R. & Yurimoto, H., 2010. Water partitioning in the Earth's mantle, *Phys. Earth planet. Inter.,* **183,** 245–251.

Ito, E. & Takahashi, E., 1989. Postspinel transformations in the system Mg_2 SiO_4-Fe_2 SiO_4 and some geophysical implications, *J. geophys. Res.,* **94**(B8), 10 637–10 646.

Jones, A.G., Fullea, J., Evans, R.L. & Muller, M.R., 2012. Calibrating laboratory-determined models of electrical conductivity of mantle minerals using geophysical and petrological observations, *Geochem. Geophys. Geosyst.,* **13**(Q06010), doi:10.1029/2012GC004055.

Karato, S., 1990. The role of hydrogen in the electrical conductivity of the upper mantle, *Nature,* **347,** 272–273.

Karato, S., 2011. Water distribution across the mantle transition zone and its implications for global material circulation, *Earth planet. Sci. Lett.,* **301,** doi:10.1016/j.epsl.2010.1.038.

Karato, S. & Wang, D., 2012. Electrical conductivity of minerals and rocks, in *Physics and Chemistry of the Deep Earth,* Chapter 5, pp. 145–182, ed. Karato, S., Wiley.

Katsura, T. *et al.*, 2007. Pressure dependence of electrical conductivity of $(Mg,Fe)SiO_3$ ilmenite, *Phys. Chem. Min.,* **34**(4), 249–255.

Katsura, T., Yoneda, A., Yamazaki, D., Yoshino, T. & Ito, E., 2010. Adiabatic temperature profile in the mantle, *Phys. Earth planet. Inter.,* **183,** doi:10.1016/j.pepi.2010.07.001.

Kelbert, A., Schultz, A. & Egbert, G., 2009. Global electromagnetic induction constraints on transition-zone water content variations, *Nature,* **460,** 1003–1007.

Khan, A. & Shankland, T.J., 2012. A geophysical perspective on mantle water content and melting: inverting electromagnetic sounding data using laboratory-based electrical conductivity profiles, *Earth planet. Sci. Lett.,* **317–318,** 27–43.

Khan, A., Connolly, J. & Olsen, N., 2006. Constraining the composition and thermal state of the mantle beneath Europe from inversion of long-period electromagnetic sounding data, *J. geophys. Res.,* **111**(B10102), doi:10.1029/2006JB004270.

Khan, A., Boschi, L. & Connolly, J., 2009. On mantle chemical and thermal heterogeneities and anisotropy as mapped by inversion of global surface wave data, *J. geophys. Res.,* **114,** B09305, doi:10.1029/2009JB006399.

Khan, A., Kuvshinov, A. & Semenov, A., 2011a. On the heterogeneous electrical conductivity structure of the Earth's mantle with implications for transition zone water content, *J. geophys. Res.,* **116,** B01103, doi:10.1029/2010JB007458.

Khan, A., Zunino, A. & Deschamps, F., 2011b. The thermo-chemical and physical structure beneath the north American Continent from Bayesian inversion of surface-wave phase velocities, *J. geophys. Res.,* **116,** B09304, doi:10.1029/2011JB008380.

Khan, A., Zunino, A. & Deschamps, F., 2013. Upper mantle compositional variations and discontinuity topography imaged beneath Australia from Bayesian inversion of surface-wave phase velocities and thermochemical modeling, *J. geophys. Res.,* **118,** 5285–5306.

Koch, S. & Kuvshinov, A., 2013. Global 3-D EM inversion of Sq-variations based on simultaneous source and conductivity determination. A concept validation and resolution studies, *Geophys. J. Int.,* **195,** 98–116.

Kohlstedt, D.L., Keppler, H. & Rubie, D.C., 1996. Solubility of water in the α, β and γ phases of $(Mg,Fe)_2$ SiO_4, *Contrib. Mineral. Petrol.,* **123,** 345–357.

Koyama, T., 2001. A study on the electrical conductivity of the mantle by voltage measurements of submarine cables, *PhD thesis,* University of Tokyo.

Koyama, T., Shimizu, H., Utada, H., Ichiki, M., Ohtani, E. & Hae, R., 2006. Water content in the mantle transition zone beneath the north Pacific derived from the electrical conductivity anomaly, in *Earth's Deep Water Cycle, AGU Geophysical Monograph,* Vol. 168, pp. 171–179, ed.Jacobsen, S.D. & van der Lee, S., American Geophysical Union.

Kustowski, B., Ekström, G. & Dziewonski, A.M., 2008. Anisotropic shear-wave velocity structure of the Earth's mantle: a global model, *J. geophys. Res.,* **113,** B06306, doi:10.1029/2007JB005169.

Kuvshinov, A.V., 2008. 3-D global induction in the oceans and solid earth: recent progress in modeling magnetic and electric fiedls from sources of magnetospheric, ionospheric and oceanic origin, *Surv. Geophys.,* **29,** 139–186.

Kuvshinov, A.V. & Olsen, N., 2006. A global model of mantle conductivity derived from 5 years of CHAMP, Ørsted, and SAC-C magnetic data, *Geophys. Res. Lett.,* **33,** L18301, doi:10.1029/2006GL027083.

Kuvshinov, A. & Semenov, A., 2012. Global 3-D imaging of mantle electrical conductivity based on inversion of observatory C-responses: I. An approach and its verification, *Geophys. J. Int.,* **189,** 1335–1352.

Kuvshinov, A.V., Avdeev, D.B., Pankratov, O.V., Golyshev, S.A. & Olsen, N., 2002. Modelling electromagnetic fields in 3D spherical Earth using fast integral equation approach, in *3D Electromagnetics,* Chapter 3, pp. 43–54, eds Zhdanov, M.S. & Wannamaker, P.E., Elsevier.

Landauer, R., 1952. The electrical resistance of binary metallic mixtures, *J. sppl. Phys.,* **23**(7), 779–784.

Litasov, K.D., 2011. Physicochemical conditions for melting in the Earth's mantle containing a C-O-H fluid (from experimental data), *Russ. Geol. Geophys.,* **52,** doi:10.1016/j.rgg.2011.04.001.

Litasov, K.D., Ohtani, E. & Sano, A., 2006. Influence of water on major phase transitions in the Earth's mantle, in *Earth's Deep Water Cycle, Geophysical Monograph Series,* Vol. **168,** pp. 95–111, eds Jacobsen, S.D. & van der Lee, S., American Geophysical Union.

Litasov, K.D., Shatskiy, A., Ohtani, E. & Katsura, T., 2011. Systematic study of hydrogen incorporation into Fe-free wadsleyite, *Phys. Chem. Miner.,* **38**(1), 75–84.

Lyubetskaya, T. & Korenaga, J., 2007. Chemical composition of Earth's primitive mantle and its variance: 1. Method and results, *J. geophys. Res.,* **112**(B3), doi:10.1029/2005JB004223.

Mookherjee, M., Stixrude, L. & Karki, B.J., 2008. Hydrous silicate melt at high pressure, *Nature,* **452,** 983–986.

Morse, P.M. & Feshbach, H., 1953. *Methods of Theoretical Physics, Part I,* McGraw-Hill.

Mosegaard, K. & Tarantola, A., 1995. Monte Carlo sampling of solutions to inverse problems, *J. geophys. Res.,* **100**(B7), 12 431–12 447.

Newman, G.A. & Alumbaugh, D., 2000. Three-dimensional magnetotelluric inversion using non-linear conjugate gradients, *Geophys. J. Int.,* **140,** 410–424.

Olsen, N., 1999. Long-period (30 days – 1 year) electromagnetic sounding and the electrical conductivity of the lower mantle beneath Europe, *Geophys. J. Int.,* **138,** 179–187.

Pankratov, O. & Kuvshinov, A., 2010. General formalism for the efficient calculation of derivatives of EM frequency domain responses and derivatives of the misfit, *Geophys. J. Int.,* **181,** 229–249.

Pankratov, O., Avdeev, D. & Kuvshinov, A., 1995. Electromagnetic field scattering in a homogeneous Earth: a solution to the forward problem., *Phys. Sol. Earth,* **31,** 201–209.

Panning, M.P. & Romanowicz, B.A., 2006. A three dimensional radially anisotropic model of shear velocity in the whole mantle, *Geophys. J. Int.,* **167,** 361–379.

Park, S.K. & Ducea, M.N., 2003. Can in situ measurements of mantle electrical conductivity be used to infer properties of partial melts? *J. geophys. Res.,* **108,** doi:10.1029/2002JB001899.

Poirier, J.-P., 2000. *Introduction to the Physics of the Earth's Interior,* 2nd edn, Cambridge Univ. Press.

Pommier, A. & Trong, E.L., 2010. 'Sigmelts: a web portal for electrical conductivity calculations in geosciences, *Comput. Geosci.,* **37,** 1450–1459.

Pommier, A., Gaillard, F., Malki, M. & Pichavant, M., 2010. Reevaluation of the electrical conductivity of silicate melts, *Am. Miner.,* **95**(2–3), 284–291.

Powell, M.J.D., 1976. Some global convergence properties of a variable metric algorithm for minimization without exact line searches, *SIAM: Am. Math. Soc. Proc.,* **9,** 53–72.

Rawlinson, N., Pozgay, S. & Fishwick, S., 2010. Seismic tomography: a window into deep Earth, *Phys. Earth planet. Inter.,* **178,** 101–135.

Roberts, J.J. & Tyburczy, J.A., 1999. Partial-melt electrical conductivity: influence of melt composition, *J. geophys. Res.,* **104,** 7055–7065.

Semenov, A. & Kuvshinov, A., 2012. Global 3-D imaging of mantle conductivity based on inversion of observatory C-responses: II. Data analysis and results, *Geophys. J. Int.,* **191,** 965–992.

Shankland, T.J. & Waff, H.S., 1977. Partial melting and electrical conductivities in the upper mantle, *J. geophys. Res.,* **82**(33), 5409–5417.

Shankland, T.J., O'Connell, R.J. & Waff, H.S., 1981. Geophysical constraints on partial melt in the upper mantle, *Rev. Geophys. Space Phys.,* **19,** 394–406.

Shimizu, H., Koyama, T., Baba, K. & Utada, H., 2010a. Revised 1-D mantle electrical conductivity structure beneath the north Pacific, *Geophys. J. Int.,* **180,** 1030–1048.

Shimizu, H., Utada, H., Baba, K., Koyama, T., Obayashi, M. & Fukao, Y., 2010b. Three-dimensional imaging of electrical conductivity in the mantle transition zone beneath the North Pacific Ocean by a semi-global induction study, *Phys. Earth planet. Inter.,* **183,** 252–269.

Simpson, F., 2001. Resistance to mantle flow inferred from the electromagnetic strike of the Australian upper mantle, *Nature,* **412,** 632–635.

Singer, B., 1995. Method for solution of Maxwell's equations in non-uniform media, *Geophys. J. Int.,* **120,** 590–598.

Smyth, J.R., 1987. β-Mg_2SiO_4 a potential host for water in the mantle? *Am. Miner.,* **72,** 1051–1055.

Smyth, J.R. & Frost, D.J., 2002. The effect of water on the 410-km discontinuity: an experimental study, *Geophys. Res. Lett.,* **29**(10), 10.1029/2001GL014418.

Song, T. R.A. & Helmberger, D.V., 2004. Low-velocity zone atop the 410-km seismic discontinuity in the northwestern United States, *Nature,* **427,** 530–533.

Tarits, P. & Mandea, M., 2010. The heterogeneous electrical conductivity structure of the lower mantle, *Phys. Earth planet. Inter.,* **183,** 115–125.

Tauzin, B., Debayle, E. & Wittlinger, G., 2010. Seismic evidence for a global low velocity layer in the Earth's upper mantle, *Nature Geosci.,* **3,** 718–721.

Toffelmier, D.A. & Tyburczy, J.A., 2007. Electromagnetic detection of a 410-km-deep melt layer in the southwestern United States, *Nature,* **441,** doi:10.1038/nature05922.

Trampert, J. & Van der Hilst, R.D., 2005. Towards a quantitative interpretation of global seismic tomography, *Geophys. Monogr.,* **60,** 47–62.

Utada, H., Koyama, T., Shimizu, H. & Chave, A.D., 2003. A semi-global reference model for electrical conductivity in the mid-mantle beneath the north Pacific region, *Geophys. Res. Lett.,* **30,** doi:10.1029/2002GL016092.

Utada, H., Koyama, T., Obayashi, M. & Fukao, Y., 2009. A joint interpretation of electromagnetic and seismic tomography models suggests the mantle transition zone below Europe is dry, *Earth planet. Sci. Lett.,* **281,** 249–257.

Vacher, P. & Verhoeven, O., 2007. Modeling the electrical conductivity of iron-rich minerals for planetary applications, *Planet. Space Sci.,* **55,** 455–466.

Velimsky, J., 2010. Electrical conductivity in the lower mantle: constraints from CHAMP satellite data by time-domain EM induction modelling, *Phys. Earth planet. Inter.,* **180**(3–4), doi:10.1016/j.pepi.2010.02.007.

Verhoeven, O. *et al.*, 2009. Constraints on thermal state and composition of the Earth's lower mantle from electromagnetic impedances and seismic data, *J. geophys. Res.,* **114,** B03302, doi:10.1029/2008JB005678.

Wang, L. & Lilley, F.E.M., 1999. Inversion of magnetometer array data by thin-sheet modelling, *Geophys. J. Int.,* **137,** 128–138.

Weidelt, P., 1972. The inverse problem of geomagnetic induction, *Z. Geophys.,* **38,** 257–289.

Wood, B.J., 1995. The effect of H_2O on the 410-kilometer seismic discontinuity, *Science,* **268,** 74–76.

Xu, Y. & Shankland, T.J., 1999. Electrical conductivity of orthopyroxene and its high pressure phases, *Geophys. Res. Lett.,* **26**(17), doi:10.1029/1999GL008378.

Xu, Y., Poe, B.T., Shankland, T.J. & Rubie, D.C., 1998. Electrical conductivity of olivine, wadsleyite, and ringwoodite under upper-mantle conditions, *Science,* **280,** 1415–1418.

Xu, Y., Shankland, T.J. & Poe, B.T., 2000. Laboratory-based electrical conductivity in the Earth's mantle, *J. geophys. Res.,* **105,** 27 865–27 875.

Yoshino, T., 2010. Laboratory electrical conductivity measurements of mantle minerals, *Surv. Geophys.,* **31,** 163–206.

Yoshino, T. & Katsura, T., 2009. Effect of iron content on electrical conductivity of ringwoodite, with implications for electrical structure in the transition zone, *Phys. Earth planet. Inter.,* **174**(1–4), 3–9.

Yoshino, T. & Katsura, T., 2012. Re-evaluation of electrical conductivity of anhydrous and hydrous wadsleyite, *Earth planet. Sci. Lett.,* **337–338,** 56–67.

Yoshino, T. & Katsura, T., 2013. Electrical conductivity of mantle minerals: role of water in conductivity anomalies, *Ann. Rev. Earth Planet. Sci.,* **41,** doi:10.1146/annurev-earth-050212-124022.

Yoshino, T., Manthilake, G., Matsuzaki, T. & Katsura, T., 2008a. Dry mantle transition zone inferred from the conductivity of wadsleyite and ringwoodite, *Nature,* **451,** 326–329.

Yoshino, T., Nishi, M., Matsuzaki, T., Yamazaki, D. & Katsura, T., 2008b. Electrical conductivity of majorite garnet and its implications for electrical structure in the mantle transition zone, *Phys. Earth planet. Inter.,* **170,** 193–200.

Yoshino, T., Matsuzaki, T., Shatskiy, A. & Katsura, T., 2009. The effect of water on the electrical conductivity of olivine aggregates and its implications for the electrical structure of the upper mantle, *Earth planet. Sci. Lett.,* **288,** 291–300.

Yoshino, T., McIsaac, E., Laumonier, M. & Katsura, T., 2012a. Electrical conductivity of partial molten carbonate peridotite, *Phys. Earth planet. Inter.,* **194–195,** doi:10.1016/j.pepi.2012.01.005.

Yoshino, T., Shimojuku, A., Shan, S., Guo, X., Yamazaki, D., Ito, E., Higo, Y. & Funakoshi, K., 2012b. Effect of temperature, pressure and iron content on the electrical conductivity of olivine and its high-pressure polymorphs, *J. geophys. Res.,* **117**(B08205), doi:10.1029/2011JB008774.

Zhang, B., Yoshino, T., Wub, X., Matsuzaki, T., Shan, T. & Katsura, T., 2012. Electrical conductivity of enstatite as a function of water content: implications for the electrical structure in the upper mantle, *Earth planet. Sci. Lett.,* **357–358,** doi:10.1016/j.epsl.2012.09.020.

APPENDIX A: DERIVATION OF GREEN'S TENSOR FOR 1-D ELECTRICAL CONDUCTIVITY STRUCTURE

Maxwell's equations in a 1-D layered Earth in the frequency domain on the spherical coordinates can be expressed as follows:

$$\nabla \times \boldsymbol{H}(\boldsymbol{r}) = \sigma(r)\boldsymbol{E}(\boldsymbol{r}) + \boldsymbol{j}(\boldsymbol{r}), \tag{A1}$$

$$\nabla \times \boldsymbol{E}(\boldsymbol{r}) = -\mathrm{i}\omega\mu_0 \boldsymbol{H}(\boldsymbol{r}), \tag{A2}$$

where $\boldsymbol{E}(\boldsymbol{r})$, $\boldsymbol{H}(\boldsymbol{r})$ and $\boldsymbol{j}(\boldsymbol{r})$ are electric field, magnetic field and electric current density of the source at the position $\boldsymbol{r}$, respectively. $\sigma(r)$ is the electrical conductivity, which is supposed to depend on only radial position r. μ_0 is the magnetic permeability of free space, a constant value. Displacement currents are ignored and dependency for time t is supposed to be $\exp(\mathrm{i}\omega t)$, where ω is angular frequency.

The aim in this section is to derive the expression of Green's tensors $G_E(\boldsymbol{r}, \boldsymbol{r}')$ and $G_H(\boldsymbol{r}, \boldsymbol{r}')$, which makes relationship between the given electric current density at a position $\boldsymbol{r}'$, $\boldsymbol{j}(\boldsymbol{r}')$ and the electric and magnetic fields at a position $\boldsymbol{r}$, $\boldsymbol{E}(\boldsymbol{r})$ and $\boldsymbol{H}(\boldsymbol{r})$, respectively, as the following:

$$\boldsymbol{E}(\boldsymbol{r}) = \int_V \mathrm{d}\boldsymbol{r}' G_E(\boldsymbol{r}, \boldsymbol{r}')\boldsymbol{j}(\boldsymbol{r}'), \tag{A3}$$

$$\boldsymbol{H}(\boldsymbol{r}) = \int_V \mathrm{d}\boldsymbol{r}' G_H(\boldsymbol{r}, \boldsymbol{r}')\boldsymbol{j}(\boldsymbol{r}'), \tag{A4}$$

where V is a volume occupied by current $\boldsymbol{j}$. $G_E(\boldsymbol{r}, \boldsymbol{r}')$ and $G_H(\boldsymbol{r}, \boldsymbol{r}')$ also depend on the electrical conductivity structure $\sigma(r)$ and an angular frequency ω.

Hereafter the source term is supposed to be $\boldsymbol{\delta}(\boldsymbol{r} - \boldsymbol{r}_0)$ instead of $\boldsymbol{j}(\boldsymbol{r})$ in eq. (A1). $\boldsymbol{\delta}(\boldsymbol{r} - \boldsymbol{r}_0)$ is one of $\delta(\boldsymbol{r} - \boldsymbol{r}_0)\hat{\boldsymbol{r}}$, $\delta(\boldsymbol{r} - \boldsymbol{r}_0)\hat{\boldsymbol{\theta}}$ or $\delta(\boldsymbol{r} - \boldsymbol{r}_0)\hat{\boldsymbol{\varphi}}$, where $\delta(\boldsymbol{r})$ is the Dirac's delta function, and $\hat{\boldsymbol{r}}$, $\hat{\boldsymbol{\theta}}$ and $\hat{\boldsymbol{\varphi}}$ are unit vectors in radial, colatitudinal and logitudinal directions, respectively. It is supposed that $\boldsymbol{r}_0 \neq \boldsymbol{0}$, that is, the source is not located at the centre of the sphere. For example, in the case that $\boldsymbol{j}(\boldsymbol{r}) = \delta(\boldsymbol{r} - \boldsymbol{r}_0)\hat{\boldsymbol{r}}$, from eqs (A3) and (A4),

$$\boldsymbol{E}(\boldsymbol{r}) = \int_V \mathrm{d}\boldsymbol{r}' G_E(\boldsymbol{r}, \boldsymbol{r}')\delta(\boldsymbol{r}' - \boldsymbol{r}_0)\hat{\boldsymbol{r}}' = G_E(\boldsymbol{r}, \boldsymbol{r}_0)\hat{\boldsymbol{r}}_0, \tag{A5}$$

$$\boldsymbol{H}(\boldsymbol{r}) = \int_V \mathrm{d}\boldsymbol{r}' G_H(\boldsymbol{r}, \boldsymbol{r}')\delta(\boldsymbol{r}' - \boldsymbol{r}_0)\hat{\boldsymbol{r}}' = G_H(\boldsymbol{r}, \boldsymbol{r}_0)\hat{\boldsymbol{r}}_0. \tag{A6}$$

In a similar manner one can write the fields for the sources with other directions,

$$\begin{pmatrix} \boldsymbol{E}(\boldsymbol{r}) \\ \boldsymbol{H}(\boldsymbol{r}) \end{pmatrix} = \begin{cases} \begin{pmatrix} G_E(\boldsymbol{r}, \boldsymbol{r}_0) \\ G_H(\boldsymbol{r}, \boldsymbol{r}_0) \end{pmatrix}\hat{\boldsymbol{r}}_0 & \text{for } \boldsymbol{j}(\boldsymbol{r}) = \delta(\boldsymbol{r} - \boldsymbol{r}_0)\hat{\boldsymbol{r}}, \\ \begin{pmatrix} G_E(\boldsymbol{r}, \boldsymbol{r}_0) \\ G_H(\boldsymbol{r}, \boldsymbol{r}_0) \end{pmatrix}\hat{\boldsymbol{\theta}}_0 & \text{for } \boldsymbol{j}(\boldsymbol{r}) = \delta(\boldsymbol{r} - \boldsymbol{r}_0)\hat{\boldsymbol{\theta}}, \\ \begin{pmatrix} G_E(\boldsymbol{r}, \boldsymbol{r}_0) \\ G_H(\boldsymbol{r}, \boldsymbol{r}_0) \end{pmatrix}\hat{\boldsymbol{\varphi}}_0 & \text{for } \boldsymbol{j}(\boldsymbol{r}) = \delta(\boldsymbol{r} - \boldsymbol{r}_0)\hat{\boldsymbol{\varphi}}. \end{cases} \tag{A7}$$

This means that to derive Green's tensors $G_E(\boldsymbol{r}, \boldsymbol{r}_0)$ and $G_H(\boldsymbol{r}, \boldsymbol{r}_0)$ is equivalent to derive $\boldsymbol{E}(\boldsymbol{r})$ and $\boldsymbol{H}(\boldsymbol{r})$ due to the source $\boldsymbol{\delta}(\boldsymbol{r} - \boldsymbol{r}_0)$.

Since $\boldsymbol{H}(\boldsymbol{r})$ is divergence free, the toroidal–poloidal decomposition can be invoked for $\boldsymbol{H}(\boldsymbol{r})$ (Backus 1986)

$$\boldsymbol{H}(\boldsymbol{r}) = \nabla \times (\nabla \times \boldsymbol{\Pi}_H(\boldsymbol{r})) + \nabla \times \boldsymbol{\Gamma}_H(\boldsymbol{r}), \tag{A8}$$

where vectors $\boldsymbol{\Pi}_H$, and $\boldsymbol{\Gamma}_H$ have only components in radial direction

$$\boldsymbol{\Pi}_H(\boldsymbol{r}) \equiv \Pi_H(\boldsymbol{r}) r\hat{\boldsymbol{r}},$$

$$\boldsymbol{\Gamma}_H(\boldsymbol{r}) \equiv \Gamma_H(\boldsymbol{r}) r\hat{\boldsymbol{r}}, \tag{A9}$$

with $\Pi_H(\boldsymbol{r})$ and $\Gamma_H(\boldsymbol{r})$ to be scalar functions of $\boldsymbol{r}$.

From eq. (A1) with the source $\boldsymbol{\delta}(\boldsymbol{r}-\boldsymbol{r}_0)$ instead of $\boldsymbol{j}(\boldsymbol{r})$ we have

$$\begin{aligned}\boldsymbol{E}(\boldsymbol{r}) &= \frac{1}{\sigma(r)}\nabla\times\boldsymbol{H}(\boldsymbol{r}) - \frac{\boldsymbol{\delta}(\boldsymbol{r}-\boldsymbol{r}_0)}{\sigma(r)} \\ &= \frac{1}{\sigma(r)}\left\{\nabla\times(\nabla\times(\nabla\times(\Pi_H(\boldsymbol{r})r\hat{\boldsymbol{r}}))) + \nabla\times(\nabla\times(\Gamma_H(\boldsymbol{r})r\hat{\boldsymbol{r}}))\right\} - \frac{\boldsymbol{\delta}(\boldsymbol{r}-\boldsymbol{r}_0)}{\sigma(r)}.\end{aligned} \tag{A10}$$

Hereafter we derive the expressions of $\Pi_H(\boldsymbol{r})$ and $\Gamma_H(\boldsymbol{r})$ instead of $\boldsymbol{E}(\boldsymbol{r})$ and $\boldsymbol{H}(\boldsymbol{r})$ themselves or $G_E(\boldsymbol{r}, \boldsymbol{r}_0)$ and $G_H(\boldsymbol{r}, \boldsymbol{r}_0)$.

The following formula can be derived (Backus 1986):

$$\nabla\times(\nabla\times(\Pi_H(\boldsymbol{r})r\hat{\boldsymbol{r}})) = (-\triangle\Pi_H(\boldsymbol{r}))r\hat{\boldsymbol{r}} + \nabla\frac{\partial(r\Pi_H(\boldsymbol{r}))}{\partial r}. \tag{A11}$$

Substituting the latter equation into eq. (A10) we obtain

$$\boldsymbol{E}(\boldsymbol{r}) = \frac{1}{\sigma(r)}\left\{\nabla\times((-\triangle\Pi_H(\boldsymbol{r}))r\hat{\boldsymbol{r}}) + \nabla\times(\nabla\times(\Gamma_H(\boldsymbol{r})r\hat{\boldsymbol{r}}))\right\} - \frac{\boldsymbol{\delta}(\boldsymbol{r}-\boldsymbol{r}_0)}{\sigma(r)}. \tag{A12}$$

Substituting eqs (A8) and (A12) into eq. (A2) we have

$$\begin{aligned}&\nabla\times\left\{\frac{1}{\sigma(r)}\nabla\times((-\triangle\Pi_H(\boldsymbol{r}))r\hat{\boldsymbol{r}})\right\} + \nabla\times\left\{\frac{1}{\sigma(r)}\nabla\times(\nabla\times(\Gamma_H(\boldsymbol{r})r\hat{\boldsymbol{r}}))\right\} \\ &= \nabla\times\{\nabla\times(-\mathrm{i}\omega\mu_0\Pi_H(\boldsymbol{r})r\hat{\boldsymbol{r}})\} + \nabla\times(-\mathrm{i}\omega\mu_0\Gamma_H(\boldsymbol{r})r\hat{\boldsymbol{r}}) + \nabla\times\left(\frac{\boldsymbol{\delta}(\boldsymbol{r}-\boldsymbol{r}_0)}{\sigma(r)}\right).\end{aligned} \tag{A13}$$

Considering the first term of the left-hand side (LHS) of eq. (A13) we write

$$\nabla\times\left\{\frac{1}{\sigma(r)}\nabla\times((-\triangle\Pi_H(\boldsymbol{r}))r\hat{\boldsymbol{r}})\right\} = \nabla\times\left\{\nabla\times\left(\frac{-\triangle\Pi_H(\boldsymbol{r})}{\sigma(r)}r\hat{\boldsymbol{r}}\right)\right\} - \nabla\times\left\{\left(\nabla\frac{1}{\sigma(r)}\right)\times((-\triangle\Pi_H(\boldsymbol{r}))r\hat{\boldsymbol{r}})\right\}. \tag{A14}$$

A vector $\nabla\dfrac{1}{\sigma(r)}$ has only a radial component and so the last term of the RHS in eq. (A14) vanishes. Thus we have

$$\nabla\times\left\{\frac{1}{\sigma(r)}\nabla\times((-\triangle\Pi_H(\boldsymbol{r}))r\hat{\boldsymbol{r}})\right\} = \nabla\times\left\{\nabla\times\left(\frac{-\triangle\Pi_H(\boldsymbol{r})}{\sigma(r)}r\hat{\boldsymbol{r}}\right)\right\}. \tag{A15}$$

Considering the second term of LHS of eq. (A13) and using the formula (A11) we write

$$\nabla\times\left\{\frac{1}{\sigma(r)}\nabla\times(\nabla\times(\Gamma_H(\boldsymbol{r})r\hat{\boldsymbol{r}}))\right\} = \nabla\times\left\{\frac{1}{\sigma(r)}(-\triangle\Gamma_H(\boldsymbol{r}))r\hat{\boldsymbol{r}}\right\} + \nabla\times\left\{\frac{1}{\sigma(r)}\nabla\left(\frac{\partial r\Gamma_H(\boldsymbol{r})}{\partial r}\right)\right\}. \tag{A16}$$

The last term of eq. (A16) is rewritten as

$$\begin{aligned}\nabla\times\left\{\frac{1}{\sigma(r)}\nabla\left(\frac{\partial r\Gamma_H(\boldsymbol{r})}{\partial r}\right)\right\} &= \nabla\times\left\{\nabla\left(\frac{1}{\sigma(r)}\frac{\partial r\Gamma_H(\boldsymbol{r})}{\partial r}\right)\right\} - \nabla\times\left\{\left(\nabla\frac{1}{\sigma(r)}\right)\left(\frac{\partial r\Gamma_H(\boldsymbol{r})}{\partial r}\right)\right\} \\ &= -\nabla\times\left\{\left(\nabla\frac{1}{\sigma(r)}\right)\left(\frac{\partial r\Gamma_H(\boldsymbol{r})}{\partial r}\right)\right\} \\ &= -\nabla\times\left\{\left(\frac{\partial}{\partial r}\frac{1}{\sigma(r)}\right)\left(\frac{\partial r\Gamma_H(\boldsymbol{r})}{\partial r}\right)\hat{\boldsymbol{r}}\right\}.\end{aligned} \tag{A17}$$

Substituting the latter result into eq. (A16) we obtain

$$\nabla\times\left\{\frac{1}{\sigma(r)}\nabla\times(\nabla\times(\Gamma_H(\boldsymbol{r})r\hat{\boldsymbol{r}}))\right\} = \nabla\times\left[\left\{\frac{-\triangle\Gamma_H(\boldsymbol{r})}{\sigma(r)} - \frac{1}{r}\left(\frac{\partial}{\partial r}\frac{1}{\sigma(r)}\right)\left(\frac{\partial r\Gamma_H(\boldsymbol{r})}{\partial r}\right)\right\}r\hat{\boldsymbol{r}}\right]. \tag{A18}$$

Substituting eqs (A15) and (A18) into eq. (A13) we have

$$\begin{aligned}&\nabla\times\left\{\nabla\times\left(\frac{-\triangle\Pi_H(\boldsymbol{r})}{\sigma(r)}r\hat{\boldsymbol{r}}\right)\right\} + \nabla\times\left[\left\{\frac{-\triangle\Gamma_H(\boldsymbol{r})}{\sigma(r)} - \frac{1}{r}\left(\frac{\partial}{\partial r}\frac{1}{\sigma(r)}\right)\left(\frac{\partial r\Gamma_H(\boldsymbol{r})}{\partial r}\right)\right\}r\hat{\boldsymbol{r}}\right] \\ &= \nabla\times\left[\nabla\times\left\{(-\mathrm{i}\omega\mu_0\Pi_H(\boldsymbol{r}))r\hat{\boldsymbol{r}}\right\}\right] + \nabla\times\left\{(-\mathrm{i}\omega\mu_0\Gamma_H(\boldsymbol{r}))r\hat{\boldsymbol{r}}\right\} + \nabla\times\left(\frac{\boldsymbol{\delta}(\boldsymbol{r}-\boldsymbol{r}_0)}{\sigma(r)}\right).\end{aligned} \tag{A19}$$

According to Helmholtz theorem, arbitrary vector can be expressed as superposition of three vectors such as a vector with only radial component, a horizontal (divergence-free) vector and a horizontal (curl-free) vector (Backus 1986)

$$\frac{\boldsymbol{\delta}(\boldsymbol{r}-\boldsymbol{r}_0)}{\sigma(r)} \equiv P(\boldsymbol{r})r\hat{\boldsymbol{r}} + \boldsymbol{\nabla}\times\left\{T(\boldsymbol{r})r\hat{\boldsymbol{r}}\right\} + \boldsymbol{\nabla}\phi(\boldsymbol{r}), \tag{A20}$$

where $P(\boldsymbol{r})$, $T(\boldsymbol{r})$ and $\phi(\boldsymbol{r})$ are scalar functions of $\boldsymbol{r}$, which should be determined. Derivation of $P(\boldsymbol{r})$ and $T(\boldsymbol{r})$ is discussed later.

Substituting eq. (A20) into eq. (A19) we have

$$\begin{aligned}&\boldsymbol{\nabla}\times\left[\boldsymbol{\nabla}\times\left\{\left(\frac{\triangle\Pi_H(\boldsymbol{r})}{\sigma(r)} - \mathrm{i}\omega\mu_0\Pi_H(\boldsymbol{r}) + T(\boldsymbol{r})\right)r\hat{\boldsymbol{r}}\right\}\right]\\ &= -\boldsymbol{\nabla}\times\left\{\left(\frac{\triangle\Gamma_H(\boldsymbol{r})}{\sigma(r)} + \frac{1}{r}\left(\frac{\partial}{\partial r}\frac{1}{\sigma(r)}\right)\left(\frac{\partial r\Gamma_H(\boldsymbol{r})}{\partial r}\right) - \mathrm{i}\omega\mu_0\Gamma_H(\boldsymbol{r}) + P(\boldsymbol{r})\right)r\hat{\boldsymbol{r}}\right\}.\end{aligned} \tag{A21}$$

A LHS and RHS of this equation are poloidal and toroidal vectors, respectively. As a poloidal vector is orthogonal with a toroidal vector (Backus 1986), this equation must be vanished. Thus it is sufficient to look for $\Pi_H(\boldsymbol{r})$ and $\Gamma_H(\boldsymbol{r})$ to satisfy two following equations:

$$\frac{\triangle\Pi_H(\boldsymbol{r})}{\sigma(r)} - \mathrm{i}\omega\mu_0\Pi_H(\boldsymbol{r}) = -T(\boldsymbol{r}), \tag{A22}$$

$$\frac{\triangle\Gamma_H(\boldsymbol{r})}{\sigma(r)} + \frac{1}{r}\left(\frac{\partial}{\partial r}\frac{1}{\sigma(r)}\right)\left(\frac{\partial r\Gamma_H(\boldsymbol{r})}{\partial r}\right) - \mathrm{i}\omega\mu_0\Gamma_H(\boldsymbol{r}) = -P(\boldsymbol{r}). \tag{A23}$$

Substituting eq. (A22) into eq. (A12) we obtain

$$\boldsymbol{E}(\boldsymbol{r}) = \frac{1}{\sigma(r)}\left\{\boldsymbol{\nabla}\times\sigma(r)(-\mathrm{i}\omega\mu_0\Pi_H(\boldsymbol{r}) + T(\boldsymbol{r}))r\hat{\boldsymbol{r}} + \boldsymbol{\nabla}\times(\boldsymbol{\nabla}\times\Gamma_H(\boldsymbol{r})r\hat{\boldsymbol{r}})\right\} - \frac{\boldsymbol{\delta}(\boldsymbol{r}-\boldsymbol{r}_0)}{\sigma(r)}. \tag{A24}$$

To reduce the original 3-D partial differential eqs (A22) and (A23) to a 1-D differential equations, spherical harmonic expansions are invoked for the functions in eqs (A22) and (A23)

$$\Pi_H(\boldsymbol{r}) \equiv \sum_{n,m}\tilde{\Pi}_n^m(r)Y_n^m(\theta,\varphi), \tag{A25}$$

$$\Gamma_H(\boldsymbol{r}) \equiv \sum_{n,m}\tilde{\Gamma}_n^m(r)Y_n^m(\theta,\varphi), \tag{A26}$$

$$T(\boldsymbol{r}) \equiv \sum_{n,m}\tilde{T}_n^m(r)Y_n^m(\theta,\varphi), \tag{A27}$$

$$P(\boldsymbol{r}) \equiv \sum_{n,m}\tilde{P}_n^m(r)Y_n^m(\theta,\varphi), \tag{A28}$$

where $Y_n^m(\theta,\varphi)$ are spherical harmonic functions of degree n and order m. $\tilde{\Pi}_n^m(r)$, $\tilde{\Gamma}_n^m(r)$, $\tilde{T}_n^m(r)$ and $\tilde{P}_n^m(r)$ are scalar functions of r. Substituting these expansions into eqs (A24) and (A8) we obtain

$$\boldsymbol{E}(\boldsymbol{r}) = \sum_{n,m}\left[\frac{1}{\sigma(r)}\{\boldsymbol{\nabla}\times\left(\sigma(r)(-\mathrm{i}\omega\mu_0\tilde{\Pi}_n^m(r) + \tilde{T}_n^m(r))Y_n^m(\theta,\varphi)r\hat{\boldsymbol{r}}\right) + \boldsymbol{\nabla}\times\left(\boldsymbol{\nabla}\times(\tilde{\Gamma}_n^m(r)Y_n^m(\theta,\varphi)r\hat{\boldsymbol{r}})\right)\}\right] - \frac{\boldsymbol{\delta}(\boldsymbol{r}-\boldsymbol{r}_0)}{\sigma(r)}, \tag{A29}$$

$$\boldsymbol{H}(\boldsymbol{r}) = \sum_{n,m}\left[\boldsymbol{\nabla}\times\left\{\boldsymbol{\nabla}\times\left(\tilde{\Pi}_n^m(r)Y_n^m(\theta,\varphi)r\hat{\boldsymbol{r}}\right)\right\} + \boldsymbol{\nabla}\times\left(\tilde{\Gamma}_n^m(r)Y_n^m(\theta,\varphi)r\hat{\boldsymbol{r}}\right)\right]. \tag{A30}$$

Thus we will derive the expression of $\tilde{\Pi}_n^m(r)$ and $\tilde{\Gamma}_n^m(r)$ instead of $\Pi_H(\boldsymbol{r})$ and $\Gamma_H(\boldsymbol{r})$. Substituting them into eqs (A22) and (A23), each mode of spherical harmonics satisfies the following equations of r:

$$\frac{1}{r^2\sigma(r)}\frac{\mathrm{d}}{\mathrm{d}r}\left(r^2\frac{\mathrm{d}}{\mathrm{d}r}\tilde{\Pi}_n^m(r)\right) - \frac{n(n+1)}{r^2\sigma(r)}\tilde{\Pi}_n^m(r) - \mathrm{i}\omega\mu_0\tilde{\Pi}_n^m(r) = -\tilde{T}_n^m(r), \tag{A31}$$

$$\frac{1}{r^2\sigma(r)}\frac{\mathrm{d}}{\mathrm{d}r}\left(r^2\frac{\mathrm{d}}{\mathrm{d}r}\tilde{\Gamma}_n^m(r)\right) - \frac{n(n+1)}{r^2\sigma(r)}\tilde{\Gamma}_n^m(r) + \frac{1}{r}\left(\frac{\mathrm{d}}{\mathrm{d}r}\frac{1}{\sigma(r)}\right)\left(\frac{\mathrm{d}r\tilde{\Gamma}_n^m(r)}{\mathrm{d}r}\right) - \mathrm{i}\omega\mu_0\tilde{\Gamma}_n^m(r) = -\tilde{P}_n^m(r). \tag{A32}$$

Therefore we should estimate $\tilde{\Pi}_n^m(r)$ and $\tilde{\Gamma}_n^m(r)$ for each n and m with a source term $\tilde{T}_n^m$ and $\tilde{P}_n^m$. Let us rewrite eqs (A31) and (A32) as follows:

$$\frac{\mathrm{d}}{\mathrm{d}r}\left(r^2\frac{\mathrm{d}}{\mathrm{d}r}\tilde{\Pi}_n^m(r)\right) - n(n+1)\tilde{\Pi}_n^m(r) - \mathrm{i}\omega\mu_0\sigma(r)r^2\tilde{\Pi}_n^m(r) = -r^2\sigma(r)\tilde{T}_n^m(r), \tag{A33}$$

$$\frac{\mathrm{d}}{\mathrm{d}r}\left(\frac{r^2}{\sigma(r)}\frac{\mathrm{d}}{\mathrm{d}r}\tilde{\Gamma}_n^m(r)\right) - \frac{n(n+1)}{\sigma(r)}\tilde{\Gamma}_n^m(r) + \left(r\frac{\mathrm{d}}{\mathrm{d}r}\frac{1}{\sigma(r)}\right)\tilde{\Gamma}_n^m(r) - \mathrm{i}\omega\mu_0 r^2\tilde{\Gamma}_n^m(r) = -r^2\tilde{P}_n^m(r). \tag{A34}$$

Eqs (A33) and (A34) are inhomogeneous Sturm–Liouville equations

$$\left\{\frac{\mathrm{d}}{\mathrm{d}r}\left(p(r)\frac{\mathrm{d}}{\mathrm{d}r}\right) + q(r) + \lambda\rho(r)\right\}\Phi(r) = -v(r), \tag{A35}$$

where $p(r)$, $q(r)$, $\rho(r)$ and $v(r)$ are functions of r, and λ is a constant. A solution of eq. (A35), $\Phi(r)$, is well known (*cf.* Morse & Feshbach 1953):

$$\Phi(r) = -y_2(r)\int_a^r \mathrm{d}r'\frac{v(r')y_1(r')}{\Delta(y_1,y_2)p(r')} - y_1(r)\int_r^b \mathrm{d}r'\frac{v(r')y_2(r')}{\Delta(y_1,y_2)p(r')}, \tag{A36}$$

where $a \le r \le b$. $y_1(r)$ and $y_2(r)$ are two general solutions of eq. (A35) with $v(r) = 0$. Note that $\Phi(r) \propto y_1(r)$ at the lower bound a, and $\Phi(r) \propto y_2(r)$ at the upper bound b. Therefore, $\Phi(r)$ follows the boundary condition of $y_1(r)$ at the lower bound a, and follows the boundary condition of $y_2(r)$ at the upper bound b. $\Delta(y_1, y_2)$ in eq. (A36) is a following Wronskian:

$$\Delta(y_1,y_2) \equiv \begin{vmatrix} y_1(r') & \mathrm{d}y_1(r')/\mathrm{d}r' \\ y_2(r') & \mathrm{d}y_2(r')/\mathrm{d}r' \end{vmatrix} = y_1(r')\frac{\mathrm{d}y_2(r')}{\mathrm{d}r'} - y_2(r')\frac{\mathrm{d}y_1(r')}{\mathrm{d}r'}. \tag{A37}$$

Note that it can be derived that $\Delta(y_1, y_2)p(r')$ is independent of r' (*cf.* Morse & Feshbach 1953).

$\Phi(r)$, $p(r)$, $q(r)$ and $v(r)$ as applied to eq. (A31), correspond to $\tilde{\Pi}_n^m(r)$, r^2, $(-n(n+1) - \mathrm{i}\omega\mu_0\sigma(r)r^2)$ and $r^2\sigma(r)T_n^m(r)$, respectively, with $\lambda = 0$. Substituting these values in eq. (A36) we have

$$\tilde{\Pi}_n^m(r) = -\tilde{\Pi}_{n,2}(r)\int_{r_\mathrm{l}}^r \mathrm{d}r'\frac{r'^2\sigma(r')\tilde{T}_n^m(r')\tilde{\Pi}_{n,1}(r')}{\Delta(\tilde{\Pi}_{n,1},\tilde{\Pi}_{n,2})r'^2} - \tilde{\Pi}_{n,1}(r)\int_r^{r_\mathrm{u}} \mathrm{d}r'\frac{r'^2\sigma(r')\tilde{T}_n^m(r')\tilde{\Pi}_{n,2}(r')}{\Delta(\tilde{\Pi}_{n,1},\tilde{\Pi}_{n,2})r'^2}, \tag{A38}$$

where $\tilde{\Pi}_{n,1}(r)$ and $\tilde{\Pi}_{n,2}(r)$ are solutions of eq. (A31) with $\tilde{T}_n^m = 0$, satisfying boundary conditions at the lower layer boundary r_l and upper layer boundary r_u, respectively. $\tilde{\Pi}_{n,1}(r)$ and $\tilde{\Pi}_{n,2}(r)$ depend on the degree n of spherical harmonics. Note also that $\Delta(\tilde{\Pi}_{n,1}, \tilde{\Pi}_{n,2})r'^2$ is constant. It is important that the formulation (A38) needs only $\tilde{\Pi}_{n,1}(r)$ and $\tilde{\Pi}_{n,2}(r)$ with a known source term $\tilde{T}_n^m$. This means that the second-order Green's tensors $G_E(r, r_0)$ and $G_H(r, r_0)$ can be expressed by using just 1-D function $\tilde{\Pi}_{n,1}(r)$ and $\tilde{\Pi}_{n,2}(r)$, and thus it is possible to reduce computational memory and efforts (*cf.* Avdeev & Knizhnik 2009).

$\Phi(r)$, $p(r)$, $q(r)$ and $v(r)$ as applied to eq. (A32), correspond to $\tilde{\Gamma}_n^m(r)$, $\frac{r^2}{\sigma(r)}$, $(\frac{-n(n+1)}{\sigma(r)} + (r\frac{\mathrm{d}}{\mathrm{d}r}\frac{1}{\sigma(r)}) - \mathrm{i}\omega\mu_0 r^2)$ and $r^2T_n^m(r)$, respectively, with $\lambda = 0$. Substituting these values in eq. (A36) we obtain

$$\tilde{\Gamma}_n^m(r) = -\tilde{\Gamma}_{n,2}(r)\int_{r_\mathrm{l}}^r dr'\frac{r'^2\tilde{P}_n^m(r')\tilde{\Gamma}_{n,1}(r')}{\Delta(\tilde{\Gamma}_{n,1},\tilde{\Gamma}_{n,2})r'^2/\sigma(r')} - \tilde{\Gamma}_{n,1}(r)\int_r^{r_\mathrm{u}} dr'\frac{r'^2\tilde{P}_n^m(r')\tilde{\Gamma}_{n,2}(r')}{\Delta(\tilde{\Gamma}_{n,1},\tilde{\Gamma}_{n,2})r'^2/\sigma(r')}, \tag{A39}$$

where $\Delta(\tilde{\Gamma}_{n,1}, \tilde{\Gamma}_{n,2})\frac{r'^2}{\sigma(r')}$ is constant. $\tilde{\Gamma}_{n,1}(r)$ and $\tilde{\Gamma}_{n,2}(r)$ are solutions of eq. (A32) with $\tilde{P}_n^m = 0$ satisfying boundary conditions at the r_l and r_u, respectively.

Finally we derive the expression of $\tilde{T}_n^m(r)$ and $\tilde{P}_n^m(r)$. Spherical harmonics expansion can be performed on the delta function $\delta(\boldsymbol{r} - \boldsymbol{r}_0)$ (*cf.* Morse & Feshbach 1953) as

$$\delta(\boldsymbol{r} - \boldsymbol{r}_0) = \frac{1}{r^2\sin\theta}\delta(r - r_0)\delta(\theta - \theta_0)\delta(\varphi - \varphi_0) = \frac{\delta(r - r_0)}{r^2}\sum_{n,m} Y_n^{m*}(\theta_0, \varphi_0)Y_n^m(\theta, \varphi), \tag{A40}$$

where $\boldsymbol{r} \equiv (r, \theta, \varphi)$ and $\boldsymbol{r}_0 \equiv (r_0, \theta_0, \varphi_0)$. A superscript $*$ indicates complex conjugate.

In the case of the source $\boldsymbol{\delta}(\boldsymbol{r} - \boldsymbol{r}_0) = \delta(\boldsymbol{r} - \boldsymbol{r}_0)\hat{\boldsymbol{r}}$, the source has only a radial component. Thus $\tilde{T}_n^m$ and $\tilde{P}_n^m$ are easily derived from eq. (A20) as follows:

$$\tilde{T}_n^m(r) = 0, \tag{A41}$$

$$\tilde{P}_n^m(r) = \frac{\delta(r - r_0)}{r^3\sigma(r)}Y_n^{m*}(\theta_0, \varphi_0). \tag{A42}$$

In the case of the source $\boldsymbol{\delta}(\boldsymbol{r} - \boldsymbol{r}_0) = \delta(\boldsymbol{r} - \boldsymbol{r}_0)\hat{\boldsymbol{\theta}}$, $\hat{\boldsymbol{r}} \cdot \nabla\times$ acts on eq. (A20). LHS of eq. (A20) is then

$$\hat{\boldsymbol{r}} \cdot \nabla \times \frac{\delta(\boldsymbol{r} - \boldsymbol{r}_0)}{\sigma(r)}\hat{\boldsymbol{\theta}} = -\frac{1}{r\sigma(r)\sin\theta}\frac{\partial\delta(\boldsymbol{r} - \boldsymbol{r}_0)}{\partial\varphi} = \frac{1}{r\sigma(r)\sin\theta_0}\frac{\partial\delta(\boldsymbol{r} - \boldsymbol{r}_0)}{\partial\varphi_0} = \sum_{n,m}\frac{\delta(r - r_0)}{r^3\sigma(r)}\frac{\partial Y_n^{m*}(\theta_0, \varphi_0)}{\sin\theta_0\partial\varphi_0}Y_n^m(\theta, \varphi). \tag{A43}$$

RHS of eq. (A20) is

$$\hat{\boldsymbol{r}} \cdot \nabla \times \left\{\nabla \times (T(\boldsymbol{r})r\hat{\boldsymbol{r}})\right\} = \sum_{n,m}\frac{n(n+1)}{r}\tilde{T}_n^m(r)Y_n^m(\theta, \varphi). \tag{A44}$$

Thus

$$\tilde{T}_n^m(r) = \frac{\delta(r-r_0)}{n(n+1)r^2\sigma(r)} \frac{\partial}{\sin\theta_0 \partial\varphi_0} Y_n^{m*}(\theta_0, \varphi_0). \tag{A45}$$

Next, $\hat{\boldsymbol{r}} \cdot \nabla \times \nabla \times$ acts on eq. (A20). LHS of eq. (A20) is

$$\hat{\boldsymbol{r}} \cdot \nabla \times \left\{ \nabla \times \left(\frac{\delta(\boldsymbol{r}-\boldsymbol{r}_0)}{\sigma(r)} \hat{\boldsymbol{\theta}} \right) \right\} = \frac{1}{r} \frac{\partial}{\partial\theta} \left[\frac{\partial}{r\partial r} \frac{r\delta(\boldsymbol{r}-\boldsymbol{r}_0)}{\sigma(r)} \right] = -\frac{1}{r} \frac{\partial}{\partial\theta_0} \left[\frac{\partial}{r\partial r} \frac{r\delta(\boldsymbol{r}-\boldsymbol{r}_0)}{\sigma(r)} \right] = \sum_{n,m} -\frac{\partial}{r^2\partial r} \left\{ \frac{\delta(r-r_0)}{r\sigma(r)} \right\} \frac{\partial Y_n^{m*}(\theta_0, \varphi_0)}{\partial\theta_0} Y_n^m(\theta, \varphi). \tag{A46}$$

RHS of eq. (A20) is

$$\hat{\boldsymbol{r}} \cdot \nabla \times \left\{ \nabla \times (P(\boldsymbol{r}) r \hat{\boldsymbol{r}}) \right\} = \sum_{n,m} \frac{n(n+1)}{r} \tilde{P}_n^m(r) Y_n^m(\theta, \varphi). \tag{A47}$$

Thus

$$\tilde{P}_n^m(r) = \frac{-1}{n(n+1)} \frac{\partial}{r\partial r} \left\{ \frac{\delta(r-r_0)}{r\sigma(r)} \right\} \frac{\partial}{\partial\theta_0} Y_n^{m*}(\theta_0, \varphi_0). \tag{A48}$$

Continuing in the similar way for $\boldsymbol{\delta}(\boldsymbol{r}-\boldsymbol{r}_0) = \delta(\boldsymbol{r}-\boldsymbol{r}_0)\hat{\boldsymbol{\varphi}}$ the following formulae can be derived:

$$\tilde{T}_n^m(r) = \frac{-\delta(r-r_0)}{n(n+1)r^2\sigma(r)} \frac{\partial}{\partial\theta_0} Y_n^{m*}(\theta_0, \varphi_0), \tag{A49}$$

$$\tilde{P}_n^m(r) = \frac{-1}{n(n+1)} \frac{\partial}{r\partial r} \left\{ \frac{\delta(r-r_0)}{r\sigma(r)} \right\} \frac{\partial}{\sin\theta_0 \partial\phi_0} Y_n^{m*}(\theta_0, \varphi_0). \tag{A50}$$

Summing up we can express $\boldsymbol{E}(\boldsymbol{r})$ and $\boldsymbol{H}(\boldsymbol{r})$ due to the source $\boldsymbol{\delta}(\boldsymbol{r}-\boldsymbol{r}_0)$, which are equivalent to Green's tensors $G_E(\boldsymbol{r}, \boldsymbol{r}_0)$ and $G_H(\boldsymbol{r}, \boldsymbol{r}_0)$, respectively, as

$$\boldsymbol{E}(\boldsymbol{r}) = \sum_{n,m} \left[\frac{1}{\sigma(r)} \left\{ \nabla \times \left(\sigma(r)(-\mathrm{i}\omega\mu_0 \tilde{\Pi}_n^m(r) + \tilde{T}_n^m(r)) Y_n^m(\theta, \varphi) r\hat{\boldsymbol{r}} \right) + \nabla \times \left(\nabla \times \left(\tilde{\Gamma}_n^m(r) Y_n^m(\theta, \varphi) r\hat{\boldsymbol{r}} \right) \right) \right\} \right] - \frac{\boldsymbol{\delta}(\boldsymbol{r}-\boldsymbol{r}_0)}{\sigma(r)}, \tag{A51}$$

$$\boldsymbol{H}(\boldsymbol{r}) = \sum_{n,m} \left[\nabla \times \left\{ \nabla \times \left(\tilde{\Pi}_n^m(r) Y_n^m(\theta, \varphi) r\hat{\boldsymbol{r}} \right) \right\} + \nabla \times \left(\tilde{\Gamma}_n^m(r) Y_n^m(\theta, \varphi) r\hat{\boldsymbol{r}} \right) \right], \tag{A52}$$

where

$$\tilde{\Pi}_n^m(r) = -\tilde{\Pi}_{n,2}(r) \int_{r_\mathrm{l}}^{r} \mathrm{d}r' \frac{r'^2 \sigma(r') \tilde{T}_n^m(r') \tilde{\Pi}_{n,1}(r')}{\Delta(\tilde{\Pi}_{n,1}, \tilde{\Pi}_{n,2}) r'^2} - \tilde{\Pi}_{n,1}(r) \int_{r}^{r_\mathrm{u}} \mathrm{d}r' \frac{r'^2 \sigma(r') \tilde{T}_n^m(r') \tilde{\Pi}_{n,2}(r')}{\Delta(\tilde{\Pi}_{n,1}, \tilde{\Pi}_{n,2}) r'^2}, \tag{A53}$$

$$\tilde{\Gamma}_n^m(r) = -\tilde{\Gamma}_{n,2}(r) \int_{r_\mathrm{l}}^{r} \mathrm{d}r' \frac{r'^2 \tilde{P}_n^m(r') \tilde{\Gamma}_{n,1}(r')}{\Delta(\tilde{\Gamma}_{n,1}, \tilde{\Gamma}_{n,2}) r'^2/\sigma(r')} - \tilde{\Gamma}_{n,1}(r) \int_{r}^{r_\mathrm{u}} \mathrm{d}r' \frac{r'^2 \tilde{P}_n^m(r') \tilde{\Gamma}_{n,2}(r')}{\Delta(\tilde{\Gamma}_{n,1}, \tilde{\Gamma}_{n,2}) r'^2/\sigma(r')}, \tag{A54}$$

$$\tilde{T}_n^m(r) = \begin{cases} 0 & \text{for } \boldsymbol{\delta}(\boldsymbol{r}-\boldsymbol{r}_0) = \delta(\boldsymbol{r}-\boldsymbol{r}_0)\hat{\boldsymbol{r}}, \\ \dfrac{\delta(r-r_0)}{n(n+1)r^2\sigma(r)} \dfrac{\partial}{\sin\theta_0\partial\varphi_0} Y_n^{m*}(\theta_0, \varphi_0) & \text{for } \boldsymbol{\delta}(\boldsymbol{r}-\boldsymbol{r}_0) = \delta(\boldsymbol{r}-\boldsymbol{r}_0)\hat{\boldsymbol{\theta}}, \\ \dfrac{-\delta(r-r_0)}{n(n+1)r^2\sigma(r)} \dfrac{\partial}{\partial\theta_0} Y_n^{m*}(\theta_0, \varphi_0) & \text{for } \boldsymbol{\delta}(\boldsymbol{r}-\boldsymbol{r}_0) = \delta(\boldsymbol{r}-\boldsymbol{r}_0)\hat{\boldsymbol{\varphi}}, \end{cases} \tag{A55}$$

$$\tilde{P}_n^m(r) = \begin{cases} \dfrac{\delta(r-r_0)}{r^3\sigma(r)} Y_n^{m*}(\theta_0, \varphi_0) & \text{for } \boldsymbol{\delta}(\boldsymbol{r}-\boldsymbol{r}_0) = \delta(\boldsymbol{r}-\boldsymbol{r}_0)\hat{\boldsymbol{r}}, \\ \dfrac{-1}{n(n+1)} \dfrac{\partial}{r\partial r} \left\{ \dfrac{\delta(r-r_0)}{r\sigma(r)} \right\} \dfrac{\partial}{\partial\theta_0} Y_n^{m*}(\theta_0, \varphi_0) & \text{for } \boldsymbol{\delta}(\boldsymbol{r}-\boldsymbol{r}_0) = \delta(\boldsymbol{r}-\boldsymbol{r}_0)\hat{\boldsymbol{\theta}}, \\ \dfrac{-1}{n(n+1)} \dfrac{\partial}{r\partial r} \left\{ \dfrac{\delta(r-r_0)}{r\sigma(r)} \right\} \dfrac{\partial}{\sin\theta_0\partial\phi_0} Y_n^{m*}(\theta_0, \varphi_0) & \text{for } \boldsymbol{\delta}(\boldsymbol{r}-\boldsymbol{r}_0) = \delta(\boldsymbol{r}-\boldsymbol{r}_0)\hat{\boldsymbol{\varphi}}. \end{cases} \tag{A56}$$

Here $\tilde{\Pi}_{n,1}(r)$ and $\tilde{\Pi}_{n,2}(r)$ are solutions $\tilde{\Pi}(r)$ of the following equation:

$$\frac{\mathrm{d}}{\mathrm{d}r} \left(r^2 \frac{\mathrm{d}}{\mathrm{d}r} \tilde{\Pi}(r) \right) - n(n+1)\tilde{\Pi}(r) - \mathrm{i}\omega\mu_0\sigma(r) r^2 \tilde{\Pi}(r) = 0, \tag{A57}$$

satisfying the boundary conditions at the lower layer boundary $r_{\rm l}$ and the upper layer boundary $r_{\rm u}$, respectively, and $\tilde{\Gamma}_{n,1}(r)$ and $\tilde{\Gamma}_{n,2}(r)$ are solutions $\tilde{\Gamma}(r)$ of the following equations:

$$\frac{\mathrm{d}}{\mathrm{d}r}\left(\frac{r^2}{\sigma(r)}\frac{\mathrm{d}}{\mathrm{d}r}\tilde{\Gamma}(r)\right)-\frac{n(n+1)}{\sigma(r)}\tilde{\Gamma}(r)+\left(r\frac{\mathrm{d}}{\mathrm{d}r}\frac{1}{\sigma(r)}\right)\tilde{\Gamma}(r)-\mathrm{i}\omega\mu_0 r^2\tilde{\Gamma}(r)=0, \tag{A58}$$

satisfying the boundary conditions at the lower layer boundary $r_{\rm l}$ and the upper layer boundary $r_{\rm u}$, respectively.

In our implementation, we assume that $\sigma(r)$ has the layered structure where $\sigma(r)$ is constant in each layer. In this case the solutions of eqs (A57) and (A58), $\tilde{\Pi}(r)$ and $\tilde{\Gamma}(r)$, are spherical Bessel functions (e.g. Banks 1969).

Note also that in numerical calculations, the degree n of spherical harmonics is truncated at some reasonable value.

APPENDIX B: QUASI-NEWTON METHOD

Quasi-Newton method is one of the algorithms to search an optimal model in unconstrained non-linear optimization problems (Fletcher 1970; Broyden *et al.* 1973). An update of the model parameter by this method is performed as follows:

$$\delta\boldsymbol{m}_k=-H_k\frac{\partial\Phi(\boldsymbol{m}_k)}{\partial\boldsymbol{m}}, \tag{B1}$$

where H_k is a matrix updated in each iteration k. A matrix H_k can be regarded as an approximation of an inverse Hessian matrix. Among a lot of algorithms to update H_k, the BFGS (Broyden–Fletcher–Goldfarb–Shanno) update based on conjugate gradients is often used. The procedure of update of the matrix H_k is as follows:

$$H_{k+1}=V_k^T H_k V_k+W_k\qquad(k=1,2,\ldots), \tag{B2}$$

where

$$V_k=I-\frac{\boldsymbol{y}_k\boldsymbol{s}_k^T}{\boldsymbol{s}_k^T\boldsymbol{y}_k}, \tag{B3}$$

$$W_k=\frac{\boldsymbol{s}_k\boldsymbol{s}_k^T}{\boldsymbol{s}_k^T\boldsymbol{y}_k}, \tag{B4}$$

$$\boldsymbol{s}_k=\boldsymbol{m}_{k+1}-\boldsymbol{m}_k, \tag{B5}$$

$$\boldsymbol{y}_k=\frac{\partial\Phi(\boldsymbol{m}_{k+1})}{\partial\boldsymbol{m}}-\frac{\partial\Phi(\boldsymbol{m}_k)}{\partial\boldsymbol{m}}. \tag{B6}$$

This formulation shows that only $\frac{\partial\Phi(\boldsymbol{m})}{\partial\boldsymbol{m}}$ is needed to update the model. Therefore a quasi-Newton method does not need additional 3-D forward calculations except for calculations of $\frac{\partial\Phi(\boldsymbol{m})}{\partial\boldsymbol{m}}$. The initial matrix H_1 can be an arbitrary positive definite matrix and may be expected to preferably be similar to the inverse Hessian matrix. Usually any *a priori* information on the inverse Hessian matrix is not given, and thus an identity matrix I is used as the initial matrix H_1. Note that the steepest descent direction is used to search the model $\boldsymbol{m}_{k+1}$ when $H_k=I$, as seen from eq. (B1).

Although a lot of computational memory must be used to store all the components of the matrix H_k, it can be reduced by expressing H_{k+1} as the recurrence relations of series $\boldsymbol{s}_k$ and $\boldsymbol{y}_k$:

$$\begin{aligned}H_{k+1}&=V_k^T H_k V_k+W_k\\&=(V_1V_2\cdots V_k)^T(V_1V_2\cdots V_k)+(V_2V_3\cdots V_k)^T W_1(V_2V_3\cdots V_k)+\cdots+(V_{k-1}V_k)^T W_{k-2}(V_{k-1}V_k)+V_k^T W_{k-1}V_k+W_k.\end{aligned} \tag{B7}$$

Therefore, from eq. (B1)

$$\begin{aligned}\delta\boldsymbol{m}_{k+1}&=-H_{k+1}\frac{\partial\Phi(\boldsymbol{m}_{k+1})}{\partial\boldsymbol{m}}\\&=W_k\boldsymbol{d}_k+V_k^T\left(W_{k-1}\boldsymbol{d}_{k-1}+V_{k-1}^T\left(W_{k-2}\boldsymbol{d}_{k-2}+V_{k-2}^T\left(\cdots+V_2^T\left(W_1\boldsymbol{d}_1+V_1^T\boldsymbol{d}_0\right)\right)\right)\right),\end{aligned} \tag{B8}$$

where

$$\boldsymbol{d}_k=-\frac{\partial\Phi(\boldsymbol{m}_{k+1})}{\partial\boldsymbol{m}}, \tag{B9}$$

$$\boldsymbol{d}_{l-1}=V_l\boldsymbol{d}_l\qquad(l=1,\ldots,k). \tag{B10}$$

This indicates that only vectors $\boldsymbol{s}_l$ and $\boldsymbol{y}_l$ $(l=1,\ldots,k)$ are needed and the operations of inner product of vectors are calculated $3\times k$ times at the most in eqs (B8) and (B10). Then when iteration number k of the inversion is much smaller than the number of model parameters which is a usual case, the BFGS update does not consume much both the computational memory and computational time.

One considers giving up information on previous search directions $\boldsymbol{s}_l$ and $\boldsymbol{y}_l$ $(l=1,\ldots,k-1)$ and then storing only two vectors $\boldsymbol{s}_k$ and $\boldsymbol{y}_k$ to save the memory. Because $\boldsymbol{m}_{j+1}$ should be the minimum point of $\Phi(\boldsymbol{m})$ in the direction of $(\boldsymbol{m}_{j+1}-\boldsymbol{m}_j)$ by the exact line search, that

is, $\boldsymbol{s}_j^T \frac{\partial \Phi(\boldsymbol{m}_{j+1})}{\partial \boldsymbol{m}} = 0$ ($j = 1, \ldots, k$), the eq. (B8) is simplified by using the first two terms,

$$\delta \boldsymbol{m}_{k+1} = W_k \boldsymbol{d}_k + V_k^T \boldsymbol{d}_{k-1}$$

$$= -\frac{\partial \Phi(\boldsymbol{m}_{k+1})}{\partial \boldsymbol{m}} + \frac{\boldsymbol{y}_k^T \frac{\partial \Phi(\boldsymbol{m}_{k+1})}{\partial \boldsymbol{m}}}{\left(\frac{\partial \Phi(\boldsymbol{m}_k)}{\partial \boldsymbol{m}}\right)^T \left(\frac{\partial \Phi(\boldsymbol{m}_k)}{\partial \boldsymbol{m}}\right)} \delta \boldsymbol{m}_k. \tag{B11}$$

This update formula is equivalent to the NLCG (Non-linear Conjugate Gradient; e.g. Newman & Alumbaugh 2000). Therefore the NLCG is regarded as an extremely limited-memory quasi-Newton method with the exact line search (Avdeev & Avdeeva 2009; Kuvshinov & Semenov 2012).

In this study we use the BFGS update rather than the NLCG, because the BFGS update has strong convergence properties. Moreover the exact line search in the BFGS update is not required (Powell 1976) thus decreasing number of calls of 3-D forward problem calculations.

In the BFGS update, it can be easily shown from eq. (B2) that if a scalar $\boldsymbol{s}_k^T \boldsymbol{y}_k$ is positive, the updated matrix H_{k+1} is guaranteed to be positive definite. Conversely if $\boldsymbol{s}_k^T \boldsymbol{y}_k$ is not positive, H_{k+1} is not positive definite because $\boldsymbol{y}_k^T H_{k+1} \boldsymbol{y}_k = \boldsymbol{y}_k^T \boldsymbol{s}_k \leq 0$ as it is seen from eq. (B2), and then eq. (B1) cannot be used. Therefore while $\boldsymbol{s}_k^T \boldsymbol{y}_k$ is not positive the steepest descent method is used instead of the quasi-Newton method, and then the quasi-Newton method is restarted after $\boldsymbol{s}_k^T \boldsymbol{y}_k$ becomes positive again.